Turkish Journal of Electromechanics & Energy

an international open access journal

SL PUBLISHING
Science Literature

www.scienceliterature.com

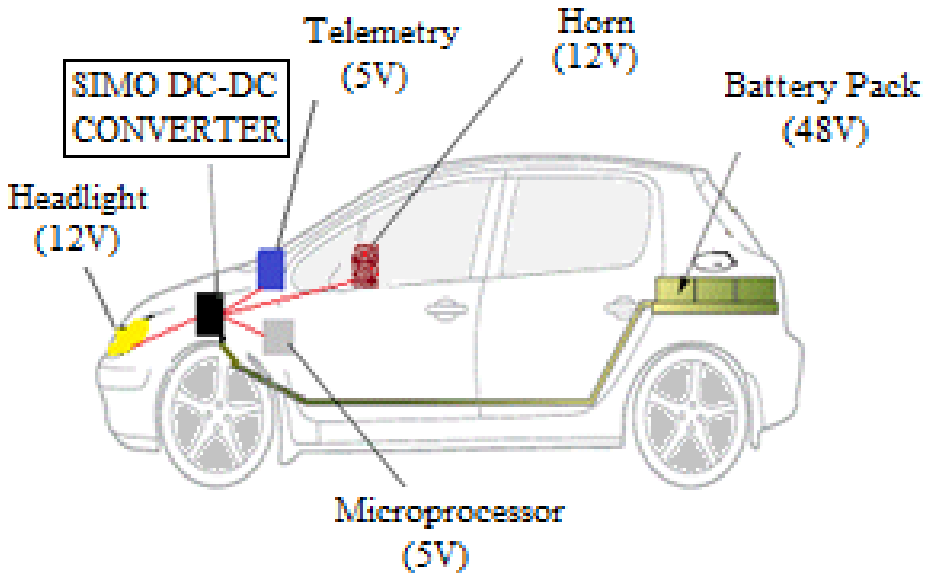

TURKISH JOURNAL OF ELECTROMECHANICS AND ENERGY
VOLUME 2 NO 2

ISSN 2547-975X

2017 July-December Issue

SCIENCE LITERATURE

Kazım Karabekir Work-Center,
F:3/C/196, 50. Year Street,
Lalapaşa Neighborhood,
Yakutiye, Erzurum, Turkey

https://www.scienceliterature.com

30.12.2017

Special Issue Article | ICADET 2017[b]

Turkish Journal of Electromechanics & Energy

ISSN-2547-975X

Contiki OS Usage in Wireless Sensor Networks (WSNs)

Erhan Sesli[1*], Gökçe Hacıoğlu[2]

[1] Sürmene Abdullah Kanca Vocational School of Higher Education, Karadeniz Technical University, Trabzon, Turkey
[2] Department of Electrical and Electronics Engineering, Karadeniz Technical University, Trabzon, Turkey

Received: 26 October 2017; Revised: 2 December 2017; Accepted: 15 December 2017; Published: 30 December 2017
Turk J Electrom Energ Vol.: 2 No: 2 Page: 1-6 (2017)
SLOI: http://www.sloi.org/
*Correspondence E-mail: erhansesli@ktu.edu.tr

ABSTRACT Wireless Sensor Networks (WSNs) have very wide range of applications from health to agriculture, from military technologies to observing of volcano activities. Developers and engineers frequently need to simulate WSN to ensure developed applications work successfully and to analyze effects of various configurations of wireless nodes. Simulating the designed scenario and embedding the designed algorithms into the wireless modules effectively are the important factors for the developers and engineers in this field. In this study, Contiki Operating System is proposed as a convenient solution for developers and engineers. Contiki is an open source, Linux based operation system, and developed for Internet of Things (IoT) devices. In this paper, primarily, Contiki OS usage and advantages in WSN were explained, then Contiki OS usage over a sample scenario was given and finally advantages of Contiki OS over other popular operation systems such as Tiny OS and Lite OS were examined. Background information on WSN and Contiki OS to build an example scenario for beginners were provided.

Keywords: Wireless Sensor Networks (WSNs), Contiki OS, Simulation

Cite this article: E. Sesli, G. Hacıoğlu, Contiki OS Usage in Wireless Sensor Networks (WSNs) Turkish Journal of Electromechanics & Energy 2(2) 1-6 (2017)

1. INTRODUCTION

The identification layer of the modern information processing system is completely related to the sensing of six physical phenomena in nature such as; mechanical, electrical, magnetic, thermal, radiation, and chemical [1]. Importance of the sensing leads to develop new approaches and systems in many fields. Wireless Sensor Networks (WSNs) are regarded as a good example to new developments and technologies in this fields.

In recent years, WSNs find applications from health to agriculture, military technologies to observing of volcano activities which have vital importance at many points [2, 3]. Many of the mentioned applications have to operate in environmental conditions that are stand-alone and energy-limited. Therefore, localization algorithms [4, 5] and novel energy-efficient clustering algorithms [6, 7] in WSNs have become popular field of studies. Undoubtedly, factors such as system simulation of WSN applications, making various configurations of nodes and embedding the algorithms into wireless nodes effectively are vital for developers. In the application development phase of the WSNs, many interfaces and programs can assist to the developers. One of the appropriate solution is the usage of Contiki OS. Contiki OS is an open-source operating system which is Linux based and developed for Internet of Things (IoT) devices [8]. It has also powerful tools for building complicated wireless communication systems. Contiki OS has been especially developed for low-powered WSN apps. In other words, it has been developed for WSN applications that are able to work with AA type batteries for years. Another specific feature of the Contiki OS is Cooja Network Simulator which provides simulation environment for developed algorithms. Contiki OS, which has an integrated structure through these features, presents researcher based solutions for WSN apps that may be developed.

In the next sections of the current paper, background information is given about WSNs and Contiki OS, then comparative assessments are provided between other alternatives, finally advantages of usage of Contiki OS are examined.

[b]*Initial version of this paper was selected from the proceedings of International Conference on Advanced Engineering Technologies (ICADET 2017) which was held in September 21-23, 2017, in Bayburt, TURKEY; and was subjected to peer-review process prior to its publication.*

2. WIRELESS SENSOR NETWORKS (WSNs)

Main purpose of the WSNs is to sense variable physical phenomena in a certain environment, then to transmit the information through wireless network [2]. Basic working mechanism of a WSN node is shown in Figure 1.

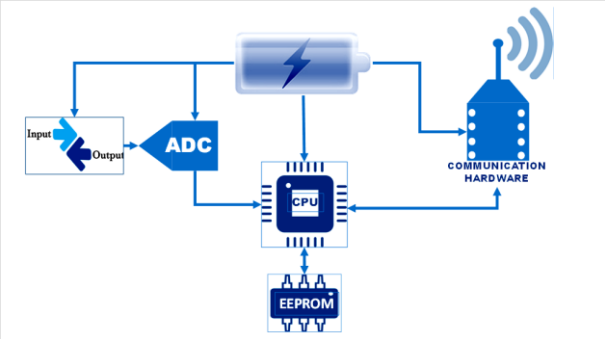

Fig. 1. Basic working mechanism of a WSN node.

A typical WSN node consists of a microprocessor, a power unit and some blocks like I/O, analog to digital converter (ADC), communication and memory block. WSNs generally operate in environmental conditions that must be stand-alone and energy-limited. Hence, power is often provided by energy harvesting methods such as solar panels, piezoelectric equipment etc. Power that is obtained by energy harvesting methods might be used for recharging the batteries.

In WSN, information is sensed by a node named as end-device, that is often at the far point in network. End-devices are manufactured as Reduced-Functioned Devices (RFDs) and have simple tasks such as sensing analog information and transmitting it. End-devices transmit information to the more authorized node in network named as Router. Routers are often manufactured as Full-Functioned Devices (FFDs). FFDs have the ability to communicate with other RFDs and FFDs. Router which is a FFD device can get information from the adjacent node and transmit it to another router or directly to the Coordinator. Coordinator which is the most authorized node in network are manufactured as FFD. Coordinator or in other words sink can be thought as the gateway of the network. General architecture of a typical WSN is shown through a scenario in Figure 2. [9].

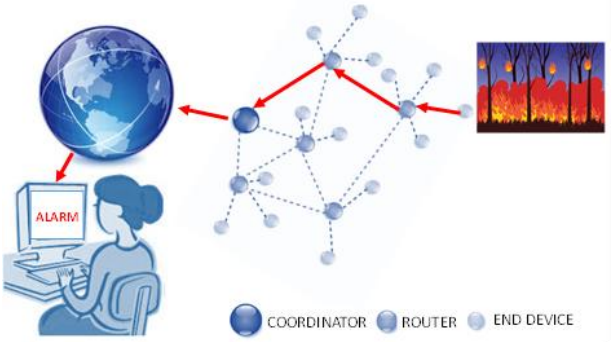

Fig. 2. General architecture of the WSNs

In the scenario, fire incidence information that occurred in a forest is sent to the end user through WSN and the internet. Primarily, fire is sensed by a sensor which is mounted to the end-device. Then, end-device transmits the information to the neighbor router. Next, information is transmitted to the coordinator by routers. After that, information which is received by coordinator is transmitted to the internet and finally the receiver gets the vital information through the internet.

Applied standards for WSNs are determined via IEEE 802.15.4 [10]. There are various available manufacturer solutions to develop applications in WSNs. Nevertheless, some of the solutions are costly. Therefore, searching cost-effective or cost-free solutions become important. On the other hand, cost-effective or cost-free solutions do not have the identical features, they have advantages/disadvantages over each other.

3. CONTIKI OPERATING SYSTEM AND ITS STRUCTURE

Contiki OS is an operating system which is developed by Dunkel et al. [11]. Contiki OS, which is C programming language based and open source, has been developed for lightweight, flexible and low-powered wireless sensor networks.

Working environments of the WSNs are often energy-limited as mentioned. This is one of the most important constraint for WSNs. Likewise, tiny and simple designs of the nodes are the other constraints. For this reason, WSNs should have some important hardware and software features to cope with these constraints. Contiki OS is one of the convenient solutions to cope with mentioned constraints thanks to its flexibility and support of lightweight and low-powered networks [11].

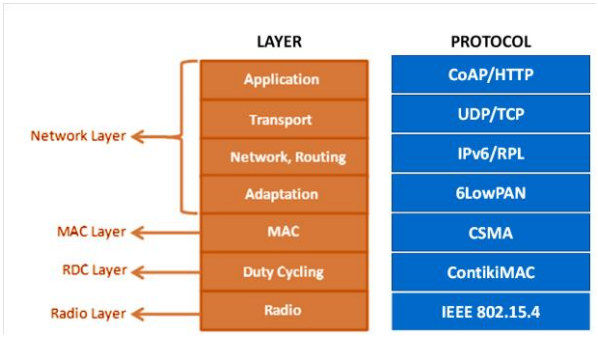

Fig. 3. Contiki network stack

A standard Contiki configuration for a microcontroller is 2kB RAM and 40 kB ROM. Besides that, Contiki can provide communication over IPv4, IPv6 and Rime Network Stack [12]. Contiki Network Stack shown in Figure 3. gives more details for its structure.

Contiki directory in OS, also provides access to system source codes, sample application codes, practical applications, and driver codes for many node types, specific microcontroller files and important tools like Cooja. Thus, besides developing and simulating new projects, Contiki provides the opportunity for developers to use existing samples directly or modify them. With these features, researchers and developers would have effective development environment.

3.1. Cooja Simulator Environment

Cooja is a WSN simulator which enables simulating the developed applications. Thus, developers can make their own applications through these codes, drivers and tools.

In Figure 4, a screenshot of Cooja environment is provided. While node communication information is flowing in colored screen which is in the middle window, node communication directions and communication ranges of the nodes can be seen on the left window.

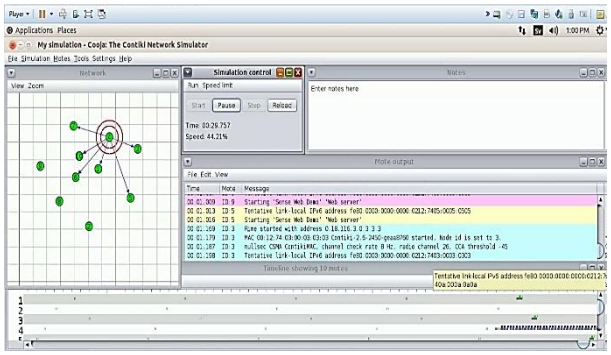

Fig. 4. A screenshot of Cooja environment

3.2. An Example in Contiki OS

Explaining the usage of Contiki OS within an example scenario will be useful for the new developers.

In the scenario three wireless nodes, one of the nodes is receiver node and the others are the energy-limited transmitter nodes, are included. Hence, transmitter nodes would sleep with certain periods for energy saving.

For this kind of example, usage of the Rime Network Stack is useful as it has a structure which makes the wireless network communication easy. If rime directory which is in Contiki OS directory is considered, codes for nodes can be built by modifying the *anonymous broadcast (abc)* sample.

For communication of receiver and transmitter nodes in given example, 25th channel (2.475 GHz) which is defined in IEEE 802.15.4 was preferred. Transmitter and receiver nodes should be configured separately. For receiver node, communication channel should be configured as 25th channel and RDC layer in Contiki Network Protocol Stack should be configured as *nullrdc*. Required configurations can be carried out by modifying the *project-conf.h* file which is in rime directory. Modified *project-conf.h* file for receiver node is given in Figure 5.

```
 * \file
 * Project specific configuration defines for th
 */
#ifndef PROJECT_CONF_H_
#define PROJECT_CONF_H_
#define NETSTACK_RADIO_RADIO_PARAM_CHANNEL 25
#define NETSTACK_CONF_RDC nullrdc_driver
#endif /* PROJECT_CONF_H_ */
```

Fig. 5. Receiver node configuration

Built code for receiver node is shown in Figure 6. Code lines that were defined by numbers include general and important details for building a project in Contiki. Code line numbers are explained as below;

1- PROCESS is one of the most important component for the Contiki. Processes are defined via PROCESS macros.

2- AUTO_PROCESS starts PROCESS automatically via the given arguments.

3- abc_recv is a function which is used to display received messages. abc_recv( ) is designated as a callback function and it is automatically called when a message is received.

4- PROCESS_THREAD is used for proto thread of a process.

5- PROCESS_EXIT HANDLER specifies an action when a process exits. In this example, quitting receiving mode is an action.

6- Beginning of the process is declared by PROCESS_BEGIN macro. It must always be in the PROCESS_THREAD definition.

7- PROCESS_END macro is used for quitting from the process.

```
#include "contiki.h"
#include "net/rime/rime.h"
#include "random.h"
#include "dev/button-sensor.h"
#include "dev/leds.h"
#include <stdio.h>
/*---------------------------------------------------------------------------*/
PROCESS(example_abc_process, "ABC example"); 1
AUTOSTART_PROCESSES(&example_abc_process);
/*---------------------------------------------------------------------------*/
static void
abc_recv(struct abc_conn *c)                                              3
{
  printf("message received'%s'\n", (char *)packetbuf_dataptr());
}
static const struct abc_callbacks abc_call = {abc_recv};
static struct abc_conn abc;
/*---------------------------------------------------------------------------*/
PROCESS_THREAD(example_abc_process, ev, data) 4
{
  static struct etimer et;

  PROCESS_EXITHANDLER(abc_close(&abc);)                                   5
  PROCESS_BEGIN();                                                        6
  abc_open(&abc, 128, &abc_call);
  PROCESS_END();                                                          7
}
```

Fig. 6. Code for receiver node

Transmitters are energy-limited nodes. They should sleep in certain intervals for energy-saving. For this reason, channel check rate of the transmitter nodes was determined as 8 times in a second. Configuration of the channel check rate provides the sleeping in certain intervals. Besides, since there are two transmitter, there may be two signal in channel at the same time. Accordingly, Radio Duty Cycle (RDC) layer in Contiki Network Protocol Stack should be configured as *contikimac*. Thus, transmitter initially listens to channel; if channel is idle then it transmits its own signal. Required configurations for these were made by changing *project-conf.h* file as seen in Figure 7. Built codes for transmitter nodes are seen in Figure 8.

```
 * \addtogroup cc2538-examples
 * @{
 *
 * \file
 * Project specific configuration defines for the
 */
#ifndef PROJECT_CONF_H_
#define PROJECT_CONF_H_
#define NETSTACK_RADIO_RADIO_PARAM_CHANNEL 25
#define NETSTACK_CONF_RDC contikimac_driver
#define NETSTACK_CONF_RDC_CHANNEL_CHECK_RATE 8
#endif /* PROJECT_CONF_H_ */
```

Fig. 7. Transmitter node configuration

```
#include "contiki.h"
#include "net/rime/rime.h"
#include "random.h"
#include "dev/button-sensor.h"
#include "dev/leds.h"
#include <stdio.h>
/*---------------------------------------------------------------------------
PROCESS(example_abc_process, "ABC example");
AUTOSTART_PROCESSES(&example_abc_process);
/*---------------------------------------------------------------------------
static void
abc_recv(struct abc_conn *c)
{
}
static const struct abc_callbacks abc_call = {abc_recv};
static struct abc_conn abc;
/*---------------------------------------------------------------------------
PROCESS_THREAD(example_abc_process, ev, data)
{
  static struct etimer et;

  PROCESS_EXITHANDLER(abc_close(&abc);)
  PROCESS_BEGIN();
  abc_open(&abc, 128, &abc_call);

  while(1) {

    etimer_set(&et, CLOCK_SECOND * 2+ random_rand() % (CLOCK_SECOND * 2));

    PROCESS_WAIT_EVENT_UNTIL(etimer_expired(&et));

    packetbuf_copyfrom("Here I am", 13);

    abc_send(&abc);

    printf("abc message sent\n");
  }

  PROCESS_END();
}
```

Fig. 8. Codes for transmitter node

A random time among 2-4 seconds was determined by *etimer_set (struct etimer*, clock_time_t)* function. Thus, event - timer was set up that time interval.

Process waits until an event occurs via *PROCESS_WAIT_EVENT_UNTIL (etimer_expired(&et))* function. When event-timer expires, event occurs and if channel is idle, *"Here I am"* information is sent as a broadcast message. Then, "*message sent*" information is written on information screen.

Written codes for nodes in scenario were compiled and scenario was built in Cooja environment. Screenshot of the scenario that was carried out in Cooja environment is provided in Figure 9.

In Figure 9 instantaneously, *sender ID2* transmits a broadcast message. While *receiver ID1* receives *"Here I am"* information, *sender ID3* waits until channel is idle. When channel goes idle, *sender ID3* transmits its own broadcast message.

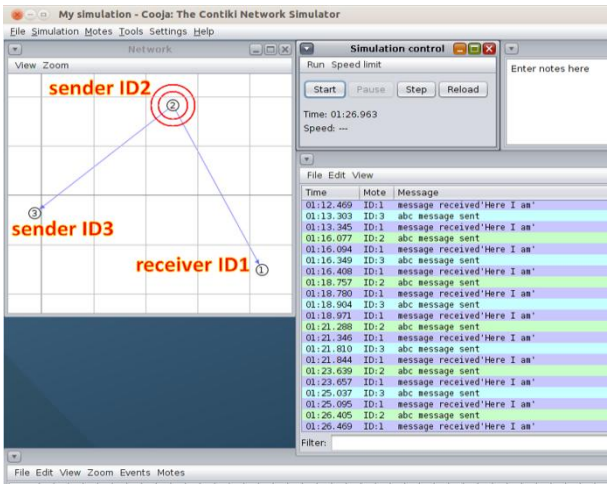

Fig. 9. Simulation in Cooja environment

In this section, general issues such as structure of the Contiki and the usage of the Contiki have been explained. In next section, other alternative WSN operating systems are explained and differences between them are examined.

4. COMPARISON OF CONTIKI OS WITH OTHER ALTERNATIVES

Other operating systems are also available for the WSNs. Among these, it can be said that Tiny OS and Lite OS are other most popular operating systems.

4.1. Tiny OS

TinyOS is a flexible and tiny operating system which consists of reusable components. Commands, events, and tasks are three computational abstractions of the components. Commands and events are used for inter-component communication. Tasks are as used to express intra-component concurrency.

Typical TinyOS configuration for a microcontroller is 16 kB ROM and 400 bytes of RAM. TinyOS has component-based programming model provided by NesC programming language. NesC language which supports features such as extensive cross-component optimizations and compile-time race detection is used in TinyOS [13].

4.2. LiteOS

LiteOS which is presented by Huawei is an open-source, interactive and Unix-like operating system for IoT devices. LiteOS is a tiny OS like others. It has 10 kB memory. As the architecture, it has three basic component as LiteC compiler, OpenSC (Open Sensor Classes) and the LiteOS runtime environment. LiteC compiler is used for compiling codes from C++ to machine language. OpenSC provides an API library to ease software development. LiteOS runtime environment presents process scheduling and resource allocation.

LiteOS has the abilities such as supporting zero configuration, auto-discovery, and auto-networking. Detailed information about LiteOS can be obtained in references [14, 15].

4.3. Comparison of Three Popular Operating Systems

Comparison among these three operating systems is shown in Table 1 [16].

When the Table 1 is examined, the following details can be observed; all three operating systems are open-source, and users can exploit them without any cost. While Contiki OS and LiteOS have dynamic system, TinyOS has the static system. In other words, Contiki OS and LiteOS are good solutions for the environment which is dynamically variable. In addition, they have flexible structure for the developers. While Contiki OS and LiteOS have the modular system, TinyOS has monolithic system. With this aspect, Contiki OS and LiteOS are more convenient for personal network applications that need to be modified frequently. From the point of network support view, Contiki OS has IPv4, IPv6 and Rime network stacks. With this features, both it is provided to communicate ability over internet for Contiki OS and presented a lightweight network stack via Rime for low-powered wireless networks. Contiki OS makes difference with its own Protothread mechanism which is a lightweight thread mechanism. Lastly, all three operating systems have their own network simulators as compared in Table 1. But Contiki OS has three different alternatives which make itself popular.

Table 1. Comparison table of the operating systems

Comparison Criterion	Contiki OS 3.0	TinyOS 2.0	Huawei LiteOS
Source model	Open source	Open source	Open source
System(Dynamic/Static)	Dynamic	Static	Dynamic
System(Monolithic/Modular)	Modular	Monolithic	Modular
Networking support	IPv4, IPv6, Rime	Active message	File-Assisted
Programming language	C	NesC	LiteC++
Multithreading support	Yes (have Protothread mechanism)	Partial (through Tiny Threads)	Yes
Simulator	Cooja, MSPSim, Netsim	TOSSIM, Power Tossim	Through AVRORA

4. CONCLUSION

In this study, primarily Contiki OS which is a lightweight, open source operating system developed for WSN application was reviewed. Then, an example scenario through Cooja in Contiki OS was explained step by step and finally a comparison with other popular operating systems such as TinyOS and LiteOS was carried out

If we scrutinize Contiki OS, it is obviously seen that it has powerful tools for building complicated wireless communication systems. Especially, Rime Network Stack is very important as it presents a lightweight network stack which is very convenient for low-powered WSN's. In addition, Protothread mechanism is one of important factors which makes difference. Likewise, flexible structure of Contiki OS and ability to use in many WSN platforms like cc2538, skymote, MicaZ, Zolertia Z1 etc. increase its preferability. This study aimed to provide background information on WSN and Contiki OS and to build an example scenario for beginners.

Acknowledgement

This study was supported by Karadeniz Technical University Scientific Research Projects Coordination Unit under Grant No: FDK-2016-5410.

References

[1] G.C.M. Meijer, Smart Sensor Systems, Wiley, Wiltshire, 55-57, (2008).

[2] D. Puccinelli, M. Haenggi, Wireless sensor networks: applications and challenges of ubiquitous sensing, IEEE Circuits and Systems Magazine, 5(3), 19-31, (2005).

[3] Y. Karan, N. As, Electromagnetic radiation measurement of a high gain wireless network adapter. Turkish Journal of Electromechanics and Energy, 1(2), 17-23, (2016).

[4] A. Pal, Localization algorithms in wireless sensor networks: Current approaches and future challenges, Network Protocols and Algorithms, 2(1), 45-73, (2010).

[5] G. Han, H. Xu, T.Q. Doung, J. Jiang, T. Hara, Localization algorithm for wireless sensor networks: A survey, Telecommunication System, 52(4), 2419-2436, (2013).

[6] M. Ye, C. Li, G. Chen, J. Wu, EECS: An energy efficient clustering scheme in wireless sensor networks, In Performance, Computing, and Communications Conference, (IPCCC 2005) 24th IEEE International, Arizona, USA, 535-540, April (2005).

[7] G. Hacioglu, V.F.A. Kand, E. Sesli, Multi objective clustering for wireless sensor networks, Expert Systems with Applications, 59, 86-100, (2016).

[8] Contiki: The open source operating system for the internet of things, 2017, http://www.contiki-os.org/

[9] K. Akkaya, M. Younis, A survey on routing protocols for wireless sensor networks. Ad hoc Networks, 3(3), 325-349, (2005).

[10] IEEE Standards 802.15.4, (2017), http://www.iith.ac.in/~tbr/teaching/docs/802.15.4-2003.pdf

[11] A. Dunkels, B. Gronvall, T. Voigt, Contiki-a lightweight and flexible operating system for tiny networked sensors, 29th Annual IEEE International Conference on Local Computer Networks, Florida, USA, 455-462, Nov. (2004).

[12] Karadeniz Technical University, Engineering Faculty, Department of Computer Engineering, Computer Networks Laboratory, (2017), http://www.ktu.edu.tr/dosyalar/bilgisayarce12e.pdf

[13] L. Philip et al., TinyOS: An operating system for sensor networks, Ambient Intelligence, Springer, 35, 115-148, (2005).

[14] Q. Cao, T. Abdelzaher, J. Stankovic, T. He, The LiteOS operating system: Towards unix-like abstractions for wireless sensor networks, In Information Processing in Sensor Networks, IPSN'08. International Conference on IEEE, St. Louis, Missouri, USA, 233-244, April (2008).

[15] Q. Cao, T. Abdelzaher, LiteOS: a lightweight operating system for C++ software development in sensor networks, In Proceedings of the 4th International Conference on Embedded Networked Sensor Systems, CO, USA, 261-262, Nov. (2006).

[16] T.V. Chien, H. N. Chan, T. N. Huu, A comparative study on operating system for wireless sensor networks, ICACSIS Conference on IEEE, Jakarta, Indonesia, 73-78, December (2011).

Biographies

Erhan Sesli was born in 1983. He received his B.Sc. degree in Electrical and Electronics Engineering from Karadeniz Technical University in 2005, Trabzon, Turkey. He worked in private sector a couple of years as telecommunication engineer. In 2012, he received his M.Sc. degree from Karadeniz Technical University Graduate School of Natural and Applied Sciences, Trabzon, Turkey. Erhan Sesli is currently a Ph.D. student at Karadeniz Technical University Graduate School of Natural and Applied Sciences. His research interests include range-based localization in wireless sensor networks (WSNs), optimization, metaheuristic algorithms and intelligent transportation systems.
E-mail: erhansesli@ktu.edu.tr

Gökçe Hacıoğlu received B.Sc. degree in Electronics Engineering from Karadeniz Technical University, Trabzon, Turkey, in 2000, the M.Sc. and Ph.D. degree in Electrical and Electronics Engineering with majors in wireless communication diversity techniques from Karadeniz Technical University Graduate School of Natural and Applied Sciences, Trabzon, Turkey in 2005 and 2011, respectively. His current research interests include diversity methods, routing algorithms of wireless sensor networks (WSNs), intelligent transport systems, visible light and power line communications and their applications in sensor networks.
E-mail: gokcehacioglu@ktu.edu.tr

Special Issue Article | ICADET 2017[C]

Turkish Journal of Electromechanics & Energy

ISSN-2547-975X

Single Input, Multiple Output DC-DC Buck Converter for Electric Vehicles

İlyass Abdillahi Aden [1*], Hakan Kahveci[1], Mustafa Ergin Şahin[2]

[1]Karadeniz Technical University, Department of Electrical and Electronics Engineering, Trabzon, 61080, Turkey
[2]Recep Tayyip Erdoğan University, Department of Electrical and Electronics Engineering, Rize, 53100, Turkey

Received: 14 November 2017; Revised 14 December 2017 Accepted: 15 December 2017; Published: 30 December 2017
Academic Editor: H. İ. Okumuş
Turk J Electrom Energ Vol.: 2 No: 2 Page: 7-13 (2017)
SLOI: http://www.sloi.org/
*Correspondance E-mail: ilyaden1992@gmail.com

ABSTRACT Increasing concerns on environmental pollution, global warming, depletion of the fossil fuel reserves and desire for reducing energy dependencies have led to an ever-increasing interest in electric vehicles (EV). The requirements for electric vehicles has brought many different problems and solutions in electric vehicle technology. One of these is the conversion of the voltage level from the battery in electric vehicles to other required voltage levels with DC-DC converters. As a solution, a separate converter can be used for each voltage level. Nevertheless, single-input multi-output (SIMO) converters can be used to reduce the cost and switching losses and hence improve system efficiency. In our study, we proposed non-isolated buck converter topology with single-input (48 V) and multi-output (12 V and 5 V). The 12 V voltage level is used for the horn, headlights while 5 V voltage level is used for the telemetry and microcontroller in electric vehicles. In this work, the general structure of a SIMO converter, design principles, small signal and stability analysis, and control steps are explained. The overall system has been simulated with Matlab / Simulink.

Keywords: Electric Vehicles, DC-DC Buck Converter, Single Input Multiple Output, Steady State Analyses, PI controller, Matlab/Simulink

Cite this article: İ. A. Aden, H. Kahveci, M. E. Şahin, Single Input, Multiple Output DC-DC Buck Converter for Electric Vehicles, Turkish Journal of Electromechanics & Energy 2(2) 7-13 (2017)

1. INTRODUCTION

Increasing demand for energy in the world and the diminishing of fossil energy sources promotes exploitation of other energy sources such as solar energy, fuel cells and other clean energy sources. These energies are usually environmentally friendly [1]. The primary utilizations of DC–DC converters include uninterruptible power supplies, battery charging/discharging devices, hybrid electric vehicle, and renewable energy systems [2-7]. Occasionally, in a typical buck converter, an active power switch replace the freewheeling diode [8–12]. A single input multiple-output DC–DC converter able of providing, boost, buck and inverted outputs at the same time has been presented in literature [13]. However, three switches are required for one output. This type of designs correspond only for low power application and output voltage. Multi-output DC–DC boost converter are studied in an another study [14]. Output voltage for high and low power applications is shared in this study. Nevertheless, for one output voltage two switches were required and its control scheme is complicated. Kumar and Omar present Single-Input Multiple-Output (SIMO) Synchronous DC-DC buck converter [15]. It has advantage of reducing the number of the switches; four switches are required for over three output voltage. Unfortunately, this SIMO converter has the disadvantage of requiring a higher current rating for four switches. Another single input, multiple outputs DC-DC converter has been proposed by Kwon, and Mora [16]. This converter is capable of providing both boost and inverted outputs. Nonetheless, in this new configuration, the loads are separately designed except the negative output. Double-output DC-DC buck converters with unidirectional and bidirectional characteristics has been presented by Santos [17]. However, the buck converter required power switches with high current ratings.

[C]*Initial version of this paper was selected from the proceedings of International Conference on Advanced Engineering Technologies (ICADET 2017) which was held in September 21-23, 2017, in Bayburt, TURKEY; and was subjected to peer-review process prior to its publication.*

This paper presents a bi-directional SIMO DC-DC buck converter for electric vehicles battery as shown in the Figure 1. The main aim of this converter is to buck the voltage coming from the battery to the different components. The presented topology has the advantage of having three switches for two outputs. In addition, the control strategies, design principles, and small signal analysis has been included. The system has been simulated in MATLAB/Simulink.

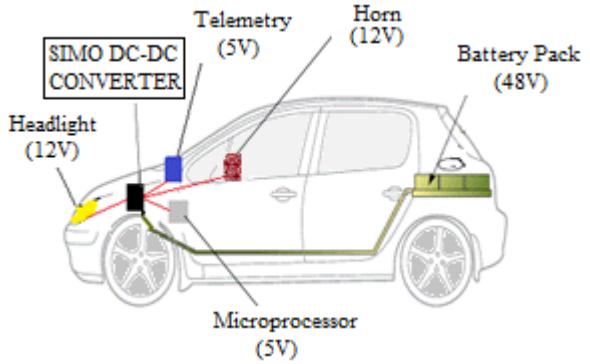

Fig. 1. SIMO DC-DC converter in electric vehicles

2. BUCK AND SIMO CONVERTER TOPOLOGY

2.1. Buck Converter

Buck converter is a step-down DC-to-DC converter, where the output voltage is lower than the input voltage [19]. The basic buck converter circuit is presented in Figure 2.

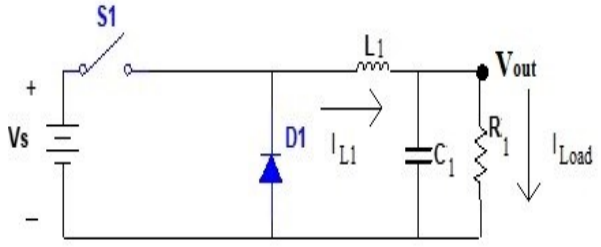

Fig. 2. Basic buck converter circuit

For the converter shown above, the current flows across the inductor in to the load when the switch (S_1) is closed. This current charges the inductor (L_1) by boosting both its magnetic field and voltage output. After a while, the output voltage (V_{out}) will attain the desired value; then the switch (S_1) is turned off and the current flows through the recovery diode (D_1). At this state, inductor (L_1) is discharged and current continues to flow through it. Before the inductor is fully discharged, the S_1 is turned on, D_1 is turned off and the cycle repeats. One can settle the ratio between the input and output voltage by modifying the duty cycle of the switch (S_1).

2.2. SIMO Converter

Single input, multiple output topology that is used in this study is given in Figure 3.b. The bi-directional DC-DC converter used in this paper has less power loss distribution among the power switches than unidirectional characteristics [12]. The topology consists of three power switches S_1; S_2 and S_3 as well as two low pass filters (L_1-C_1 and L_2- C_2) as illustrated in Figure 3.b. The state of the switches is represented as *switch x* = OFF (0) and *switch x* = ON. Since there are three switches and two states for each switch, we obtain eight ways of operating of the presented converter [11]. Three switching states are operational, only. The other combinations were not included in this work. Table I presents the topological states (TS) of the system designed.

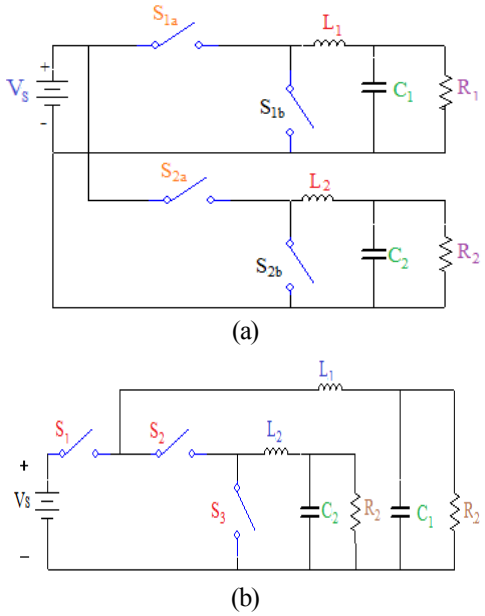

Fig. 3. Bi-directional SIMO DC-DC buck converter: (a) Parallel solution, (b) Implemented solution

The different switching states of SIMO converter are shown in Figure 4. It can be observed from the Figure 4 that:

-*In state TS-1:* Switch 1 = 1, Switch 2 = 1 and Switch 3 = 0. The input voltage (V_s) supplies energy to the loads and to the inductors, in this state both L_1 as well as L_2 is charged.

- *In state TS-2*: Switch 1 = 1, Switch 2 = 0 and Switch 3 =1. The input voltage (V_s) supplies energy to R_1–L_1 and current of the inductor L_2 (i_{L2}) flows across S_2, delivering some of its energy to the load R_2. In this circumstance, inductance L_1 and L_2 will be respectively charged and discharged.

- *In state TS-3*: Switch 1 = 0, Switch 2 = 1 and Switch 3 =1. The current in the inductor L_1 (i_{L1}) flows to both S_2 and S_3, while i_{L2} flows only across S_3, delivering its stored energy to both loads R_1 and R_2. In this situation the inductor L_1, as well as the inductor L_2 are discharged.

Table 1. Topological states of the used SIMO converter

Topological states	TS-1	TS-2	TS-3
Switch 1	ON	ON	OFF
Switch 2	ON	OFF	ON
Switch 3	OFF	ON	ON

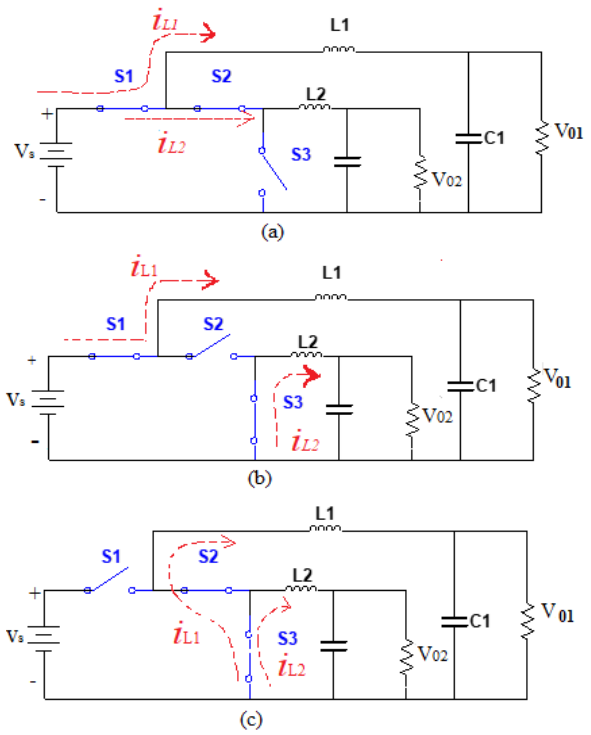

Fig. 4. The different switching states of the SIMO converter: (a) TS-1, (b) TS-2, (c) TS-3

3. STEADY STATE ANALYSIS

The presented SIMO converter is devised to operate in continuous conduction mode (CCM). The current and voltage waveforms of inductors are presented in Figure 5. T_{ON1} and T_{ON2} are the periods which the PWM generators one and two are generating the logic "1" at their corresponding outputs.

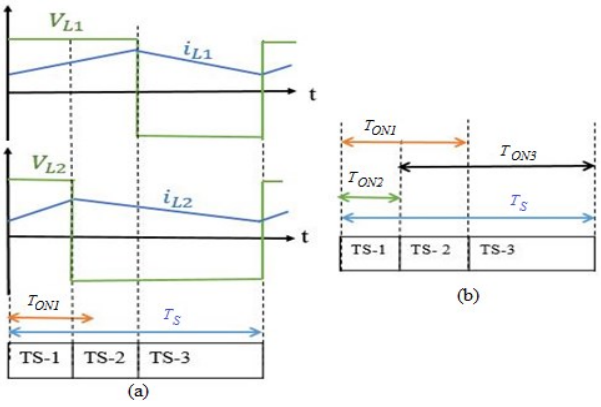

Fig. 5. Steady-state analysis of the SIMO converter; (a) Inductors current and voltage related with topological states, (b) Times in which the switch S_1, S_2 and S_3 are turned ON.

From the topological states and waveforms found in the foregoing section, it can be inferred that the output voltage V_{01} and V_{02} controls voltage V_{R1} and V_{R2} respectively. Noting that the average inductor voltage is zero, the following equations are written:

$$(V_S - V_{01}) * T_{ON1} = V_{01} * (T_S - T_{ON1}) \quad (1)$$

$$(V_S - V_{02}) * (T_S - T_{ON3}) = V_{02} * T_{ON3} \quad (2)$$

According to the equations (1, 2), the different output voltages come out as a function of their input voltage and duty cycles. V_{01} and V_{02} are expressed in the following equations:

$$V_{01} = (D_1)V_S \quad (3)$$

$$V_{02} = (1 - D_2)V_S \quad (4)$$

where D_1 and D_2 represent the duty cycles of the system.

4. GENERALIZED STATE-SPACE AVERAGE MODEL

The voltage and the current dynamics are described by the state space average and it is given in (5)-(8):

$$L_1 \frac{di_{L1}}{dt} + Vo_1 = D_1 Vs \quad (5)$$

$$C_1 \frac{dV_{01}}{dt} = i_{L1} - \frac{V_{01}}{R_1} \quad (6)$$

$$L_2 \frac{di_{l2}}{dt} + Vo_2 = D_2 Vs \quad (7)$$

$$C_2 \frac{dV_{02}}{dt} = i_{L2} - \frac{V_{02}}{R_2} \quad (8)$$

By using these equations and the state equation, the transfer functions obtained between the output voltages and the duty ratios are as follows:

$$Tp_1(s) = \frac{V_S D_1 R_1}{(R_1 C_1 L_1 s^2 + L_1 s + R_1)} \quad (9)$$

$$Tp_2(s) = \frac{V_S D_2 R_2}{(R_2 C_2 L_2 s^2 + L_2 s + R_2)} \quad (10)$$

The circuit component's values are calculated as follow:
- Output 1: For P_1= 150W/12V, V_S=48, R_1=1Ω, L_1=180µF, C_1=20µF.
- Output 2: For P_2= 25W/5V, V_S=48, R_2 =1Ω, L_2=89µF, C_2=62µF.

In the open loop the circuit transfer function with their numerical values are found as follows:

$$Tp_1(s) = \frac{12}{(3.6*10^{-9}s^2 + 180*10^{-6}s + 1)} \quad (11)$$

$$Tp_2(s) = \frac{5}{(5.5*10^{-9}s^2 + 62*10^{-6}s + 1)} \quad (12)$$

5. SIMULATION AND RESULTS

5.1. Simulink Model of SIMO DC-to-DC Converter

The simulation model of the whole system is shown in Figure 6. The system is composed of two PWM block, one logic block and the SIMO converter. The input voltage of the converter is 48 volt and the output is composed of 5 and 12 volts.

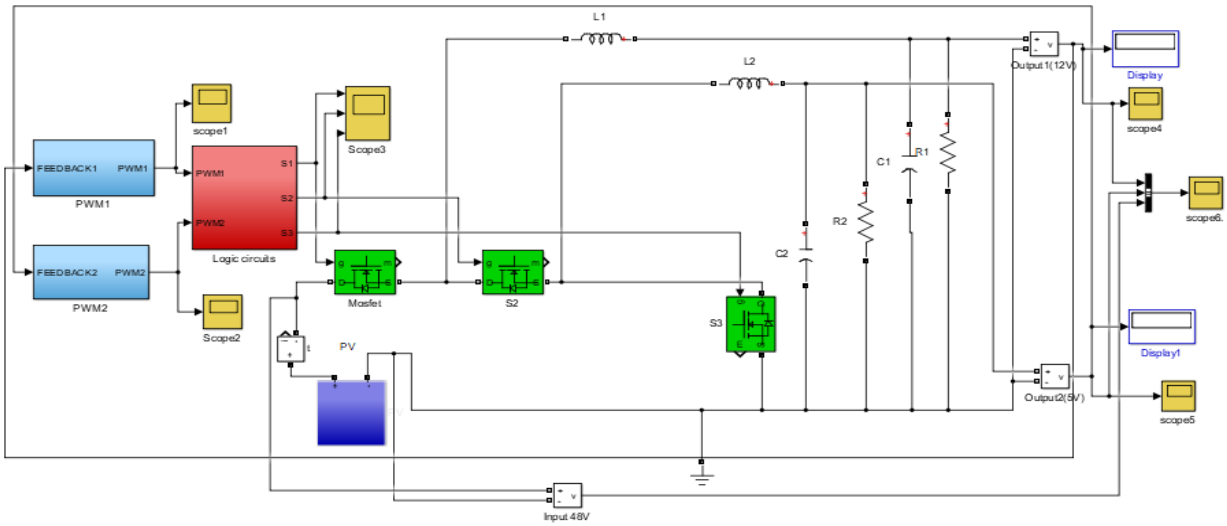

Fig. 6. Simulink diagram of the SIMO DC-DC converter

5.1.1. PWM Generator Implementation and PI Controller

All three switches discussed are controlled using PWM, and this block include PI controller. The Simulink model is given in Figure 7. DC-to-DC converters use switches to change the DC from one level to another [20]. The system operates at 50 kHz with an output value between 0 and 1. The PWM1 and PWM2 generators produce an error signal and inserted into the PI block. The output of the PI block is compared to the sawtooth. Thus, logic 1 and 0 values are produced. The PI controller is a proportional-integral controller. In our case, we used PI to control the output voltage coming from the SIMO DC-DC buck converter [18, 21]. The values of the gains K_P, and K_I, are chosen carefully using Routh–Hurwitz stability criterion. The output would reach the reference value with a very short settling time and without an overshoot.

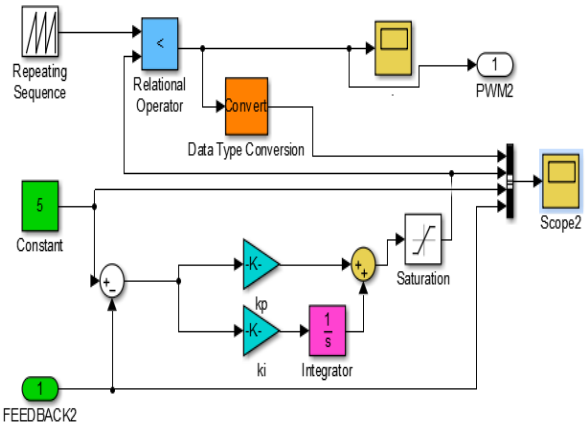

Fig. 7. PWM and PI design with Matlab/Simulink

5.1.2 Modelling the Logic Circuits

The outputs of the PWM1 and PWM2 which is illustrated in Figure 7 straightly go through a logic circuit (LC) block as given in Figure 6. This LC block command the state of the switches S_1, S_2 and S_3. From the topological states point of view (shown in Table I), it can be deduced that the charging of the inductor L_1 is fully reliant to switch 1 (S_1), consequently to control V_{O1} the PWM1 is directly connected to S_1. In contrary, either charging or discharging of L_2 is not reliant on the state of S_2 since when the L_2 is discharging in the TS-3 the switch S_2 is ON. The second PWM generator defines an interval that the switch S2 should begin to operate. In addition, switch S_2 should be controlled in such a way that prohibited states are avoided. These requirements are achieved by using a two input "OR" gate and a "NOT" gate shown. Lastly, the other two switches specify the switch S3. This deduces that the only work for the switch S_3 to avoid the prohibited states. This is achieved using NAND gate. The logic block is shown in Figure 8(a) and the gate signals of S_1, S_2 and S_3 are presented in Figure 8(b).

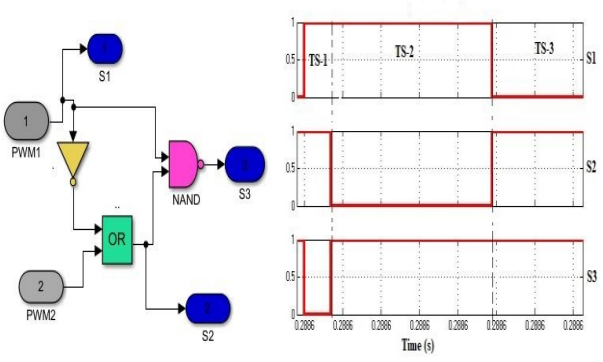

(a) (b)

Fig. 8. Gate signals of the switches: (a) Logic block; (b) Output signals of the block

5.2. SIMO DC-DC Converter Represented with Transfer Function

The simulation diagram of single input, multiple output (SIMO) converter along with transfer function presented in this paper and the results are shown respectively in Figures (9, 10).

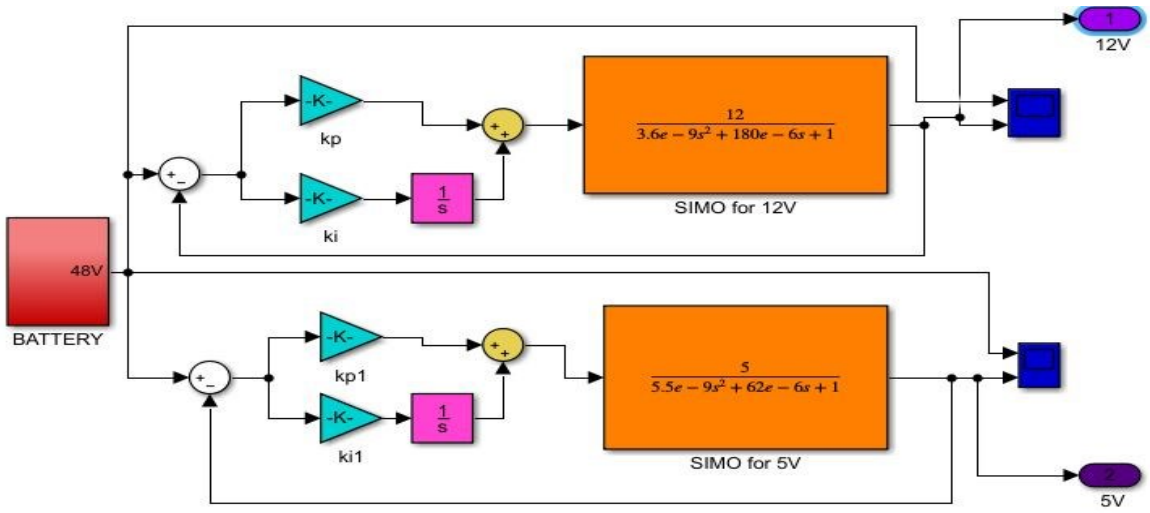

Fig. 9. SIMO converter with transfer function diagram

Figure 10 shows the simulation results of the transfer function of DC-DC converter. It can be deduced that all outputs reach their values in short time.

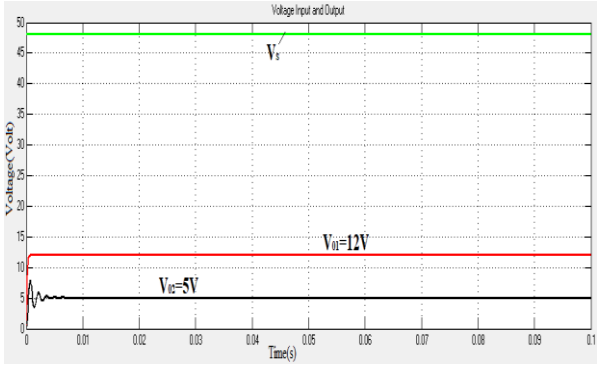

Fig. 10. The SIMO DC-DC converter

The PI controller continuously detect an error signal as the difference between feedback loop and the reference voltage. During the first zone, the feedback signal (black line) is less than the reference value (green line) as seen in the Figure 11, so error is negative. The PI controller produces signal (red color line) to eliminate the difference between feedback and reference and the switch S_1 is ON. During this period, the PWM generate pulses. In the second section, the feedback is higher than reference of 12 V, so error is positive. The PI is not generating a signal and the switch S_1 is OFF.

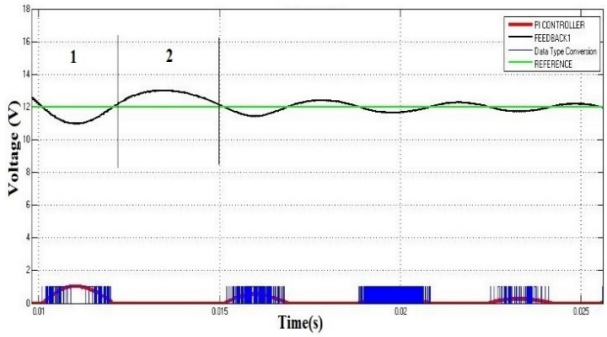

Fig. 11. Working principle of PI controller designed with Matlab/Simulink

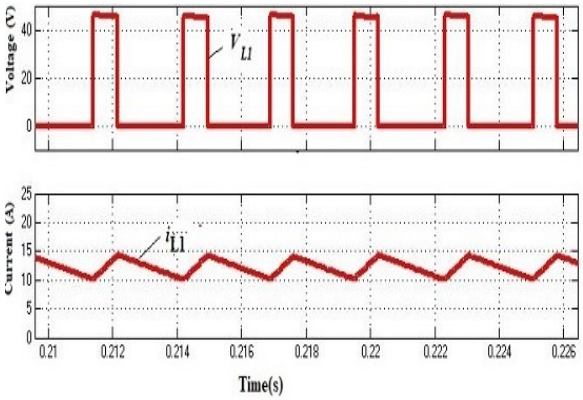

(a)

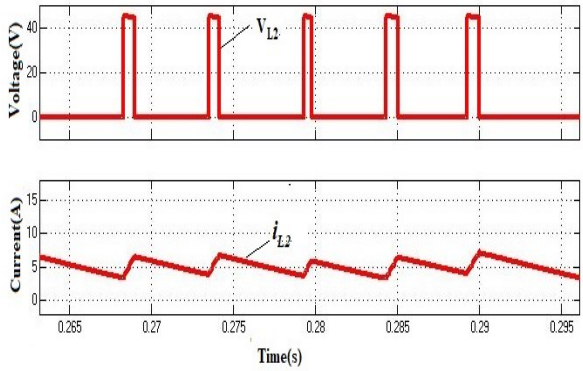

(b)

Fig. 12. Voltage and current associated with each inductor: (a) Variables of the inductor L_1, (b) Variables of the inductor L_2

The Simulink model of the SIMO DC-DC converter is given in Figure 13. Adding that all the required output voltages reaches their values with a very small overshoot.

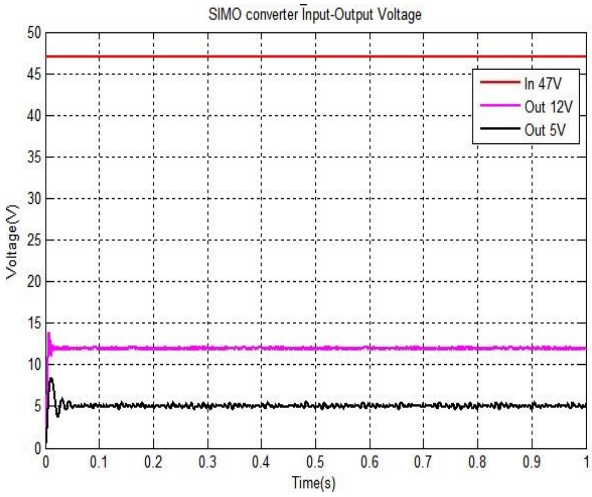

Fig. 13. Input and output voltages of SIMO DC-DC converter

Current in the load R_1 and R_2 is shown respectively in Figure 14 (a, b) when both loads are equal to 1Ω. When load is increased to R_1= R_2 =1.5 Ω, one can observe that the output current decrease as shown in Figure 15 (a, b). This implies that the output currents depend on the load. When the load is increased, the current decreases. The same when the load decreases, the current increases.

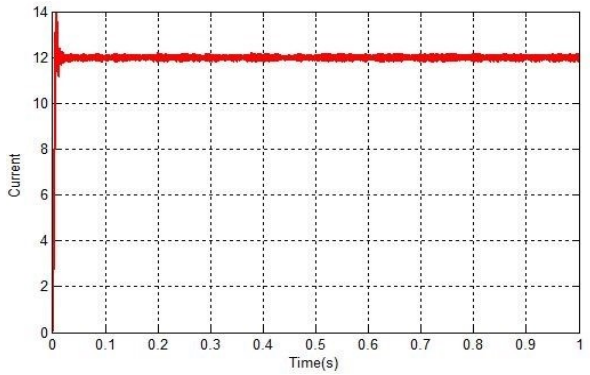

(a)

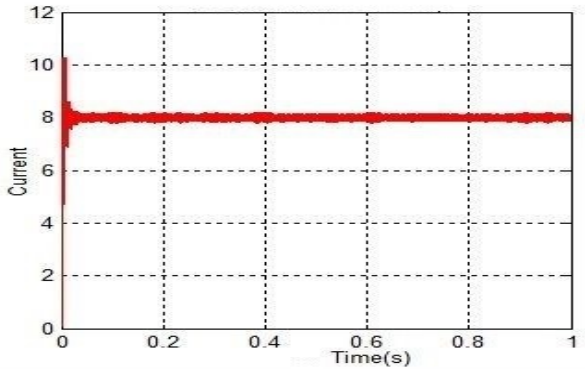

(b)

Fig. 14. The current as a function of loads: (a) Load R_1=1 Ω (b), Load R_2=1 Ω

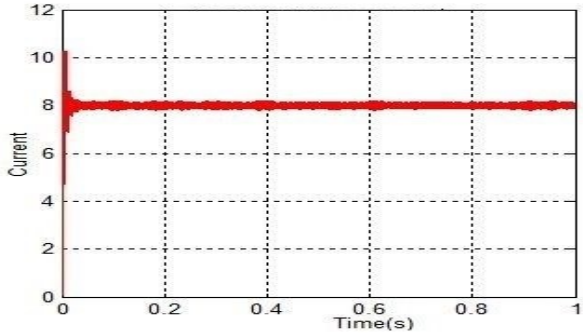

(a)

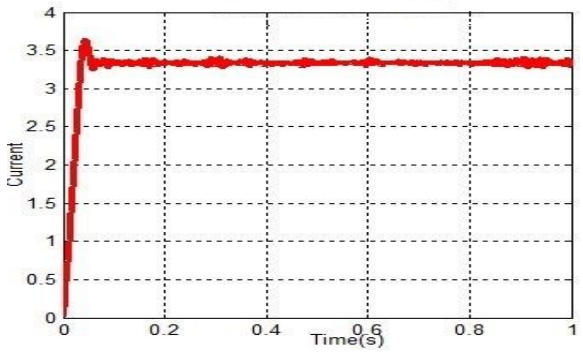

(b)

Fig. 15. The current as a function of loads: (a) Load R_1=1.5 Ω (b), Load R_2=1.5 Ω

6. CONCLUSION

In this study, we have used single-input, multiple-output converter that can be used for electric vehicles. Steady state analysis of the models, control strategies and PWM implementations are presented. The simulation of the both dynamic model and static model is performed in Matlab/Simulink. Simulink results show that this converter is suitable for the electrical vehicles. The idea of using only one converter that can supply power for different voltage output requirements is not far away. Efforts continue to realize single-input multiple-output buck converter more efficient in their control schemes and cost-effective for the integration of electric vehicles, renewable energy systems, mobile equipments, batteries and other applications.

References

[1] P. U. Sanchis, and L. Marroyo, Adaptive voltage control of the DC/DC boost stage in PV converters with small input capacitor, IEEE Trans. Power Electron., 28(11), 5038–5048, (2013).

[2] D. G. Chatterjee, and B. Fernandez, Modified soft-switched three-phase three-level DC–DC converter for high-power applications having extended duty cycle range, IEEE Trans. Ind. Electron., 59(9), 3362–3372, (2012).

[3] N. M. L. Tan, T. Abe, and H. Akagi, Design and performance of a bidirectional isolated DC–DC converter for a battery energy storage system, IEEE Trans. Power Electron., 27(2), 1237–1248, (2012).

[4] Z. Ouyang., Z. Zhang, O. C. Thomsen, and M.A.E Andersen, Planar-integrated magnetics (PIM) module in hybrid bidirectional DC–DC converter for fuel cell application, *IEEE* Trans. Power Electron. 26, (11), 3254–3264, (2011).

[5] Z. Zhang, Z. Ouyang, O.C. Thomsen, and M.A.E. Andersen, Analysis and design of a bidirectional isolated DC–DC converter for fuel cells and supercapacitors hybrid system, IEEE Trans. Power Electron, 27(2), 848–859, (2012).
[6] K. J. Ruan, K. Yang, and M. Xu, Power management for fuel cell power system cold start, IEEE Trans. Power Electron., 24(10), 2391–2395, (2009).
[7] L. Wang, Z. Wang, and H. Li, Asymmetrical duty cycle control and decoupled power flow design of a three-port bidirectional DC–DC converter for fuel cell vehicle application, IEEE Trans. Power Electron, 27(2), 891–904, (2012).
[8] V. A. Babazadeh, B. Ramachandran, L. Pao, D. Maksimovic, and E. Alarcon, Proximate time optimal digital control for synchronous buck dc-dc converters, IEEE Transaction on Power Electronics, 23(4), 2018–2026, (2008).
[9] F. Lee, K. Yao, M. Xu, and M. Ye, Tapped-inductor buck converter for high-step-down DC-DC conversion, IEEE Transaction on Power Electronics, 20, 775–780, (2005).
[10] D. Maksimovic, and X. Zhang, Multimode digital controller for synchronous buck converters operating over wide ranges of input voltages and load currents, IEEE Transaction on Power Electronics, 25(8), 1958–965, (2010).
[11] K. Yao, Y. Qiu, M. Xu, and F. Lee, A novel winding coupled buck converter for high frequency, high-stepdown dc-dc conversion, IEEE Transaction on Power Electronics, 20, 1017–1024, (2005).
[12] Y. Y. Mai, and P. Mok, A constant frequency output ripple-voltage-based buck converter without using large ESR capacitor, IEEE Trans. Circuits and Systems II, 55, 748–752, (2008).
[13] P. Patra, A. Patra, and N. Misra, A single inductor multiple output switcher with simultaneous buck, boost, and inverted outputs, IEEE Trans. Power Electron., 27(4), 1936–1951, (2012).
[14] A. Nami, F. Zare, A. Ghosh, and F. Blaabjerg, Multiple-output DC–DC converters based on diode-clamped converters configuration: Topology and control strategy, IET Power Electron., 3(2), 197–208, (2010).
[15] B. K. Sabbarapu, O. Nezamuddin, A. McGinnis, and E. dos Santos. Single-input multiple-output synchronous DC-DC buck converter, IEEE Energy Conversion Congress and Exposition (ECCE), (2016).
[16] D. Kwon, and G. A. R. Mora, Single-Inductor–Multiple-Output Switching DC–DC Converters, IEEE transactions on circuits and systems—ii: express briefs, 56(8), (2009).
[17] E. C. D. Santos, Dual-output DC-DC Buck converters with bidirectional and unidirectional Characteristics, IET Transactions on Power electronics, 6(5), 999–1009, (2013).
[18] M. S. Ebrahim, A. M. Sharaf, A. M. Atallah, and A. S. Emareh, An Efficient Controller for Standalone Hybrid-PV Powered System, Turkish Journal of Electromechanics and Energy, 2(1), (2017).
[19] M. A. El-Sharkawi, Fundamentals of Electric Drives, CI-Engineering, (2.Edition), 68-73, (2000).
[20] N. Mohan, Converters, Applications, and Design, John Wiley and sons Inc., (2. Edition), 161-200, (1995).
[21] Q. Leu, J. W. Jung, T. D. Do, E. K. Kim, H. H. Choi, Adaptive PID Speed Control Design for Permanent Magnet Synchronous Motor Drives, IEEE Transaction on Power Electronics, 30(2), 900-908, (2015).

Biographies

Ilyass Abdillahi Aden was born in Djibouti. He received his University Diploma of Technology in Industrial Engineering and Maintenance, and B.Sc applied in industrial maintenance from University of Djibouti, in 2013 and 2014 respectively. He is currently graduate student pursuing M.Sc. degree in the Department of Electrical and Electronics Engineering in KTU, Trabzon. His research interests include power electronics and renewable energy.

E-mail: ilyaden1992@gmail.com.

Hakan Kahveci was born in Kırşehir, Turkey. He received his B.Sc degree in Electrical Engineering and Ph.D degree from Karadeniz Technical University (KTU), Turkey, in 2006 and 2013, respectively. He is currently an assistant professor in Electrical and Electronics Engineering Department at KTU. He has been a member of the Chamber of Electrical Engineers in Turkey. He works on electrical machine control systems and power electronics.

E-mail: hknkahveci@ktu.edu.tr

Mustafa Ergin Şahin was born in, 1978 in Trabzon, Turkey. He received his B.Sc. degree in Electrical & Electronics Engineering from Karadeniz Technical University (KTU), M.Sc. degree from Gazi University in Ankara and Ph.D. degree from KTU, Trabzon, Turkey, in 2002 and 2006, 2014, respectively. He is currently an assistant professor in Electrical and Electronics Engineering Department at RTE University. He was worked at different projects on low voltage power systems and relay manufacturer for power systems. He is an active reviewer for scientific journals in the field. He is also member of the Chamber of Electrical Engineers in Turkey. His main research interests are power electronics and utilization of renewable energy.

E-mail: mustafaerginsahin@yahoo.com

Special Issue Article | Submit Manuscript[ŧ]

Turkish Journal of Electromechanics and Energy

ISSN: 2547-975X

Production of AA 2024 Aluminum Alloy Ribbons by Melt Spinning Process

Sultan ÖZTÜRK[1], Sefa Emre SÜNBÜL[1*], Kürşat İCİN[1], Bülent ÖZTÜRK[1]

[1]Department of Metallurgical and Materials Engineering, Karadeniz Technical University, Trabzon, TURKEY

Received: 10 October 2017; Revised: 28 November 2017 Accepted: 17 December 2017; Published: 30 December 2017

Turk J Electrom Energ Vol.: 2 No: 2 Page: 14-19 (2017)

SLOI: http://www.sloi.org/

*Correspondence E-mail: sunbulsefa@ktu.edu.tr

ABSTRACT In this study, rapidly solidified AA2024 aluminum ribbons were produced with laboratory scale melt spinning device by using different wheel speeds. The alloy was melted with induction furnace under high vacuum atmosphere. The influence of the wheel speed on the dimensions and cooling rates of produced ribbons was examined. The produced ribbons had 20–80 µm thickness, 1–4 mm width, and 10–60 mm length. Increasing wheel speed from 28 to 43 m/s resulted in decreasing ribbon thickness from 79 µm to 24 µm. Microhardness measurements were also performed and it was noted that the hardness values changed with wheel speed (35–39 $HV_{0.01}$).

Keywords: AA2024 Aluminum Alloy, Rapid Solidification, Melt Spinning

Cite this article: S. Öztürk, S. E. Sünbül, K. İcin, B. Öztürk, Production of AA 2024 Aluminum Alloy Ribbons by Melt Spinning Process, Turkish Journal of Electromechanics & Energy 2(2) 14-19 (2017)

1. INTRODUCTION

Rapid solidification is a commonly used method and frequently used to manufacture superior metals and alloys either by rapid quenching or by sub-cooling [1]. In general, this technique can be defined as the fast extraction of thermal energy of metals or alloys from liquid state to solid state at room temperature. The metal in the liquid state is very short in contact with the cold surface, causing instant supercooling to occur in the liquid metal over 100°C during the solidification [2].

Rapid solidification can be achieved by carrying out one of the below criteria;

1. Realization of excessive cooling before solidification,
2. Achieve a high speed in the line of solidification,
3. Achieve a high cooling rate on the sidelines of solidification.

The initial condition requires supercooling or over-cooling of molten metal or alloy to the temperature that the latent heat is estranged completely from the solidifying mass, before being delivered to ambient environment. The next condition to impose rapid solidification is to move solidifying metal or alloy with very high speed during solidification drawing a thin specimen. Finally, high cooling rate is the most popular method used in rapid solidification methods. The main difference among these three techniques is that the rapid cooling is included in all stages in third method, but rapid cooling takes place just in the line of solidification in first two methods. High cooling rates allows influential conduction of thermal energy in all stages of solidification process. The main parameter to achieve high cooling rate is to reduce at least one size of solidifying metal or alloy and exposing the alloys to high heat subtraction rates [2].

There are several various rapid solidification techniques for production of superior metals. The most widespread technique is the melt spinning method. This method is nowadays standard in industrial applications for producing different dimensions of ribbons. Rapid solidification of the liquid metal in the form of ribbon is achieved by using a metal disk rotating at high speed and having high thermal conductivity in this method [3, 4]. There are many production parameters that affect the

[ŧ]*Initial version of this paper was selected from the proceedings of International Conference on Advanced Engineering Technologies (ICADET 2017) which was held in September 21-23, 2017, in Bayburt, TURKEY; and was subjected to peer-review process prior to its publication.*

physical and mechanical properties of the produced ribbons such as wheel speed, liquid metal temperature, distance between nozzle and wheel surface, ejecting gas pressure and nozzle geometry [5, 6]. Among these variants, wheel speed is the most important factor [7].

The mechanical properties of aluminum and its alloys depend on purity of adding alloying elements. It is necessary to change the microstructure of the alloy to enhance the properties [8, 9]. Aluminum based intermetallic systems have important features such as; high melting point, low density, optimum chemical resistance [10]. For example, in Al-Cu alloy systems mechanical properties such as strength, hardness, fatigue and creep resistances mainly depend on copper addition [11]. AA2024 aluminum alloys are used in different areas which require high temperature, high strength, low density, low weight, fair workability, fair corrosion resistance, ductility, fatigue resistance, machinability and heat-treatability [9, 12, 13].

While various studies in literature dedicated to Al based alloys, the microstructural developments and microhardness of undercooled AA2024 alloys have not been explored. Al-Cu alloys found variety of applications in aircraft, aerospace, electronics and automotive industries. The goal of the current study is to examine the effect of the wheel speed on the undercooled ribbons' shape and to determine the effects of rapid solidification and cooling rate on the microstructural, mechanical (hardness) properties.

2. EXPERIMENTAL

The material used in this study is AA2024 aluminum alloy with the nominal composition given in Table 1. The experimental works have been carried out at laboratory scale single roller melt spinning device working in vacuum condition as shown in Figure 1. In order to study the effect of the wheel speed on dimension, microstructure and microhardness of the ribbons, a number of experiments have been performed, in which wheel speed was changed while other parameters were kept constant.

Each run was started with melting of AA2024 aluminum alloy ingot in boron nitride crucible having rectangular slit shape. The slit shape nozzle with the size of 7x0.8 mm was used. Four different wheel speeds 28, 34, 39 and 43 $m.s^{-1}$ were employed to study the effect of wheel speed on the size of ribbons. Gap distance from the tip of the nozzle to the wheel surface was set to 1 mm. High purity argon gas (99.999%) was used to eject the molten metal on the wheel and the ejection pressure of the gas was kept 75 kPa during all experiments. Ribbons were produced with constant melt temperature of 1023 K and a pyrometer (thermometer) located near the crucible was used to monitor the melt temperature. The chamber of the melt spinning apparatus has been evacuated before each run. When the melt temperature reached the expected temperature, molten metal was ejected by applying a pressurized gas through the slit nozzle on the rotating copper wheel as the ribbon shape.

The microstructure and surface properties of produced ribbons were examined with a scanning electron microscope of Zeiss EVO MA model. The hardness measurements of the ribbons were performed with a NOVA 130/240 (INNOVATEST, Maastricht the Netherlands) model digital microhardness tester at room temperature. Vickers pyramidal indenter with 0.01 kg and 5 seconds of holding time were employed.

Table 1. Chemical composition of AA2024 (ASTM B209-14)

Elements	% weight
Cu	3.8-4.9
Mg	1.2-1.8
Mn	0.3-0.9
Fe	0.5
Si	0.5
Zn	0.25
Ti	0.15
Cr	0.10
Al	Balance

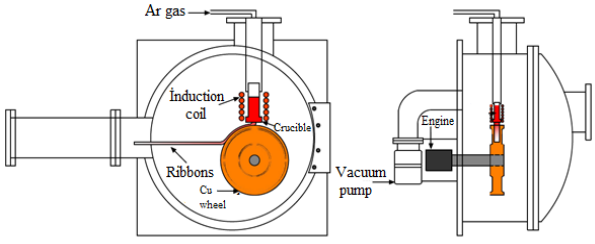

Fig. 1. Schematic diagram of melt spinning system

3. RESULTS

Figure 2 shows macro image of the melt spun AA2024 aluminum alloy ribbons produced with wheel speeds of 28, 34, 39 and 43 $m.s^{-1}$. As it can be seen from the figure, discontinuous ribbons with the sizes of 20–78 μm in thickness, 1–4 mm in width, and 10–60 mm in length were produced. It is also seen from

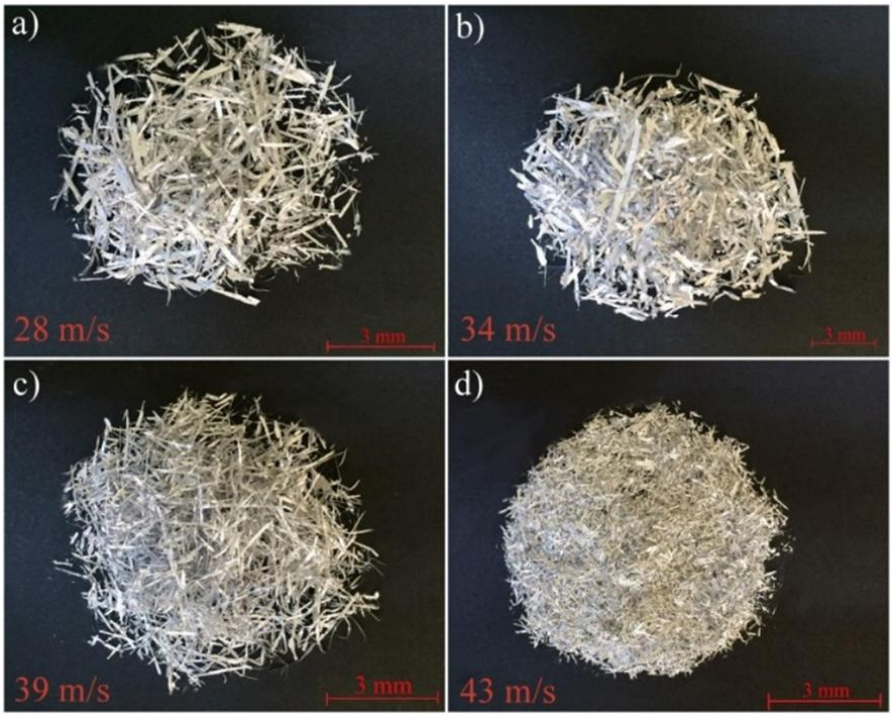

Fig. 2. Macrograph of discontinuous ribbons produced with different wheel speeds. Wheel speeds: a) 28 m/s, b) 34 m/s, c) 39 m/s and d) 43 m/s

the figure that the sizes of the ribbons decreased with increasing wheel speed. Among the size parameters, the ribbon thickness is the most important factor that effects the cooling rate and microstructure of the ribbons. From this perspective, the effect of wheel speed on the thickness was studied in a detailed manner. Figure 3 demonstrates the variation of thickness parameter of melt-spun ribbons as a function of the wheel speed. During these processes, as stated above, ejection pressure of 75 kPa, melt temperature of 1023 K, and nozzle-wheel distance of 1 mm were kept constant. As it can be seen from the Figure 3, the ribbon thickness decreased significantly with increasing wheel speed. For wheel speeds of 28, 34, 39 and 43 $m.s^{-1}$, the average ribbon thicknesses are recorded as 70 µm, 52 µm, 40 µm and 24 µm, respectively. Beyond 43 m/s wheel speed, the ribbon shape starts to convert into powder shape. This can be explained by increasing centrifugal energy given to the liquid metal to break up [10, 14]. The SEM micrographs of the produced ribbons had two different surface morphologies on the wheel side and air side are shown in Figure 4 and Figure 5, respectively. The wheel side surface of the ribbons is relatively smooth and has air pockets due to existence of poor heat transfer between the wheel and melted alloy [15]. The air side of the ribbons has rough surface with metal flow lines parallel to melt flow direction.

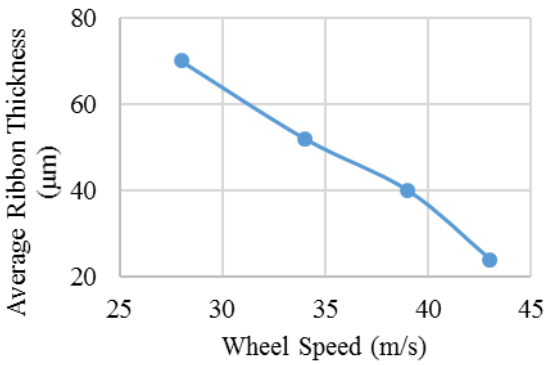

Fig. 3. The variation of the ribbon thickness with wheel speed

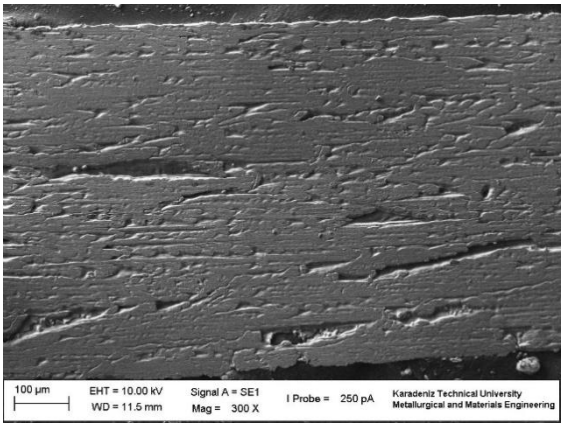

Fig. 4. SEM micrographs of wheel side surface of produced ribbons (at wheel speed of 28 m/s)

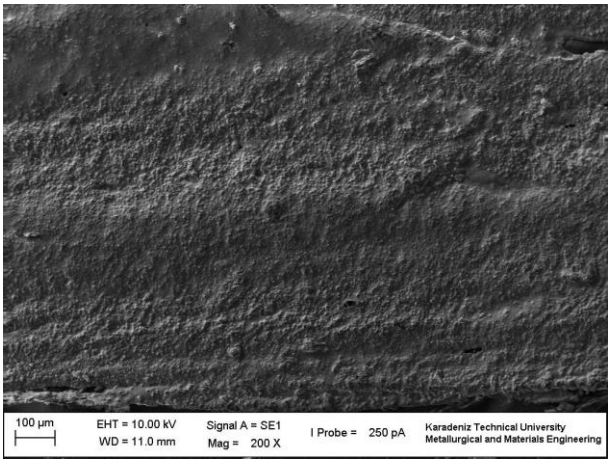

Fig. 5. SEM micrographs of air side surface of produced ribbons (at wheel speed of 28 m/s)

Figure 6 and Figure 7 show the SEM images of the microstructure for melt spun ribbons produced with 28 and 39 m/s wheel speeds, respectively. As it can be seen from the figures, the microstructures of the ribbons were characterized by fine-grained structure. The average grain size decreased with increasing wheel speed. The average grain sizes were measured as 15 µm and 12 µm for ribbons produced at wheel speeds of 28 m/s and 39 m/s, respectively.

Cooling rates and dendrite arm spacing depending on wheel speed for AA2024 were calculated. Some empirical equations were suggested by different authors to estimate the cooling rate of aluminum-copper alloys. Sarreal and Abbaschian [16] indicated cooling rates of the Al-4.9Cu alloy by Equation 1. The calculation of the cooling rates in this study was based on Equation 1;

$$DAS = 46.6 \times \varepsilon^{-0.29} \quad (1)$$

where, DAS represents the dendrite arm spacing or average grain size in µm, and ε stands for the cooling rate in K/s.

The variation of average grain size and cooling rate values depending on ribbon thickness is evaluated. Cooling rate becomes 49.83 K/s while average grain size is about 15 µm for 28 m/s wheel speed and it is 107.58 K/s for average grain size of 12 µm at 39 m/s wheel speed.

The key goal of this paper was to work the fabrication of undercooled Al–Cu alloy ribbons by using melt-spinning method and determine relationships between wheel speed and microhardness of AA2024 alloy. Hardness test is applied to determine the mechanical properties of rapid solidified ribbons. One of these tests, the Vickers hardness (Hv) is the ratio of the load applied to the brale to the surface area of the indentation. The hardness value is calculated using the Vickers formula [11, 17].

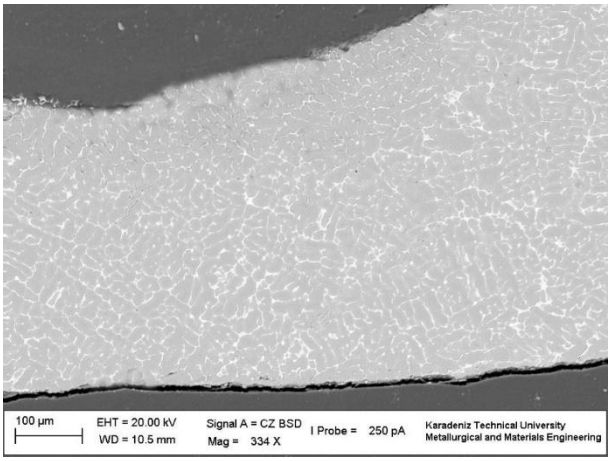

Fig. 6. Microstructure of AA2024 aluminum alloy melt spun ribbons produced with 28 m/s wheel speed

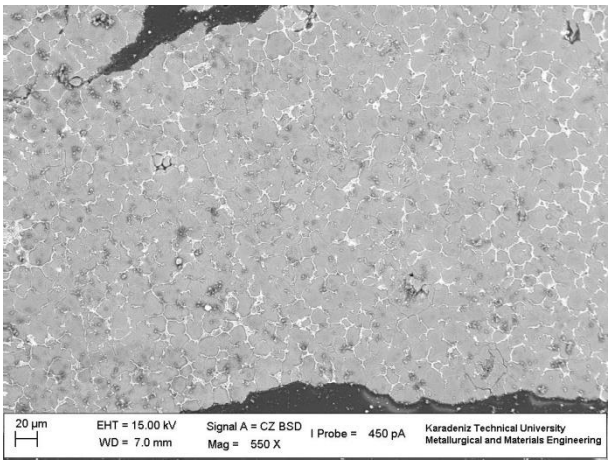

Fig. 7. Microstructure of AA2024 aluminum alloy melt spun ribbons produced with 39 m/s wheel speed

$$H_V = \frac{2Psin(\frac{\theta}{2})}{d^2} \quad (2)$$

where P is the applied load (kg), d the mean diagonal of the indentation (mm), θ the angle between opposite faces of the diagonal brale (136°).

In this work, the mechanical properties of produced ribbons were determined by Vickers microhardness measurement. The measured microhardness values were given in Figure 8. The average values were measured as 35.13, 36.14, 38.78, and 39.40 $HV_{0.01}$, for wheel speeds of 28 m/s, 34 m/s, 39 m/s, and 43 m/s, respectively. As it can be seen from the figure, the increasing wheel speed barely enhances microhardness values [18, 19].

The grain sizes of rapidly solidified ribbons produced with higher wheel speed is smaller than that for low-speed ribbons. This increase in hardness values can be explained by the reduction of the average grain size due to increased cooling rate with increasing wheel speed [3, 20]. Minor change in microstructure results minimal effect from 35 to 39 $Hv_{0.01}$ in microhardness.

In other respects, the microhardness values of the produced ribbons at the highest wheel speed 43 m/s are

slightly higher. The reason for that the microstructure of this ribbon is clearly finer than others. These results show the homogeneous distribution of the microstructure and the average grain size greatly affect the hardness of the undercooled ribbons.

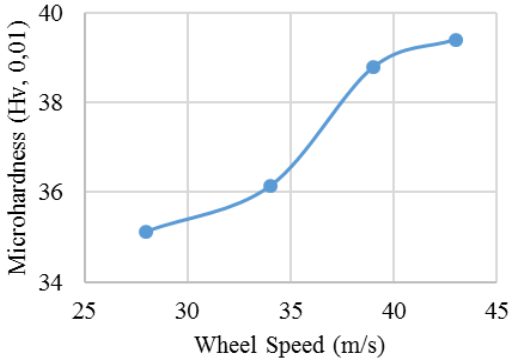

Fig. 8. The effect of wheel speed on microhardness of produced ribbons

4. CONCLUSION

The rapidly solidified AA 2024 aluminum alloy ribbons were produced with the single roller melt spinning method and the size and microstructural properties of the ribbons changed with wheel speed. The following conclusions were drawn from the present results;

- AA2024 aluminum alloy ribbons with discontinuous form were produced with melt spinning method and the sizes of the ribbons such as length, width, and thickness decreased with increasing wheel speed.
- Microstructure of the produced ribbons was characterized by equiaxed grains and the average grain sizes decreased with increasing wheel speed.
- Microhardness of the produced ribbons increased with decreasing ribbon thickness.

References

[1] J. Gao, B. Wei, Containerless solidification of undercooled NdFeZrB alloy droplets in a drop tube, Journal of Alloys and Compounds, 285(1), 229-232, (1999).

[2] E. J. Lavernia, T. S. Srivatsan, The rapid solidification processing of materials: science, principles, technology, advances, and applications, Journal of Materials Science, 45(2), 287-325, (2009).

[3] M. Gögebakan, O. Uzun, T. Karaaslan, M. Keskin, Rapidly solidified Al–6.5 wt.% Ni alloy, Journal of Materials Processing Technology, 142(1), 87-92, (2003).

[4] M. Kramer, Solidification, microstructural refinement and magnetism in Nd2Fe14B, Journal of Magnetism and Magnetic Materials, 241(1), 144-155, (2002).

[5] S. Sarafrazian, A. Ghasemi, M. Tavoosi, Magnetic characterization of nanocrystalline Fe14Nd2B1 alloy during melt spinning and subsequent annealing, Journal of Magnetism and Magnetic Materials, 402, 115-123, (2016).

[6] K. Simeonidis, C. Sarafidis, E. Papastergiadis, M. Angelakeris, I. Tsiaoussis, O. Kalogirou, Evolution of Nd2Fe14B nanoparticles magnetism during surfactant- assisted ball-milling, Intermetallics, 19(4), 589-595, (2011).

[7] M. Srinivas, B. Majumdar, G. Phanikumar, D. Akhtar, Effect of planar flow melt spinning parameters on ribbon formation in soft magnetic Fe68.5Si18.5B9Nb3Cu 1 alloy, Metallurgical and Materials Transactions B, 42(2), 370-379, (2011).

[8] L. Katgerman, F. Dom, Rapidly solidified aluminum alloys by meltspinning, Materials Science and Engineering: A, 375-377, 1212-1216, (2004).

[9] P. C. Varley, The technology of aluminum and its alloys. CRC Press, 1970.

[10] E. Karaköse, M. Keskin, Structural investigations of mechanical properties of Al based rapidly solidified alloys, Materials & Design, 32(10), 4970-4979, (2011).

[11] W. R. Osorio, J. E. Spinelli, I. L. Ferreira, A. Garcia, The roles of macro segregation and of dendritic array spacings on the electrochemical behavior of an Al-4.5 wt.% Cu alloy, Electrochimica Acta, 52(9), 3265-3273, (2007).

[12] K. S. Ghosh, M. Hilal, S. Bose, Corrosion behavior of 2024 Al-Cu-Mg alloy of various tempers, Transactions of Nonferrous Metals Society of China, 23(11), 3215-3227, (2013).

[13] B. Rebba, N. Ramanaiah, Evaluation of Mechanical Properties of Aluminum Alloy (Al-2024) Reinforced with Molybdenum Disulphide (MoS_2) Metal Matrix Composites, Procedia Materials Science, 6, 1161-1169, (2014).

[14] V. I. Tkatch, A. I. Limanovskii, S. N. Denisenko, S. G. Rassolov, The effect of the melt-spinning processing parameters on the rate of cooling, Materials Science and Engineering: A, 323(1–2), 91-96, (2002).

[15] R. Seino, Y. Sato, Observation of melt puddle behavior in planar flow casting in air, Journal of Alloys and Compounds, 586(1), S150-S152, (2014).

[16] J. A. Sarreal, G. J. Abbaschian, The Effect of Solidification Rate on Microsegregation, (in English), Metallurgical Transactions a-Physical Metallurgy and Materials Science, 17(11), 2063-2073, (1986).

[17] Y. F. Song, Effects of two-stage aging on the dimensional stability of Al-Cu-Mg alloy, Journal of Alloys and Compounds, 701, 508-514, (2017).

[18] E. Karaköse, M. Keskin, Microstructure properties and microhardness of rapidly solidified Al64Cu20Fe12Si4 quasicrystal alloy, Metals and Materials International, 18(2), 257-263, (2012).

[19] E. Karaköse, M. Keskin, Investigation of microstructural, mechanical and thermal properties of rapidly solidified Ni–7 wt% Si alloy, Materials Science and Engineering:A, 553, 181-191, (2012).

[20] E. Karaköse, M. Keskin, Effect of solidification rate on the microstructure and microhardness of a melt-spun Al–8Si–1Sb alloy, Journal of Alloys and Compounds, 479(1–2), 230-236, (2009).

Biographies

Sultan ÖZTÜRK was born in Trabzon, Turkey. He holds B.Sc. degree in manufacturing engineering from Gazi University, M.Sc. degree in agriculture machines from Akdeniz University and Ph.D. degree in mechanical engineering from Karadeniz Technical University (KTU). He is currently professor in Metallurgical and Materials Engineering Department at KTU. His research interests cover rapid solidification, aluminum alloys, magnetic materials, neodymium magnets and powder metallurgy.
E-mail: suozturk@ktu.edu.tr

Sefa Emre SÜNBÜL was born in İzmir and obtained B.Sc. degree in Metallurgical and Materials Engineering from KTU in 2011. He completed M.Sc. in the Department of Metallurgical and Materials Engineering of KTU in 2015. He is currently a research assistant in the Institute of Science and Technology at KTU. His main research interests are rapid solidification, aluminum alloys and energy storage materials.
E-mail: sunbulsefa@ktu.edu.tr

Kürşat İCİN was born in Kırklareli and graduated from KTU in 2012. He obtained M.Sc. degree from Metallurgical and Materials Engineering Department KTU in 2016. He is currently a research assistant in the Institute of Science and Technology at KTU. His current research areas include rapid solidification, magnetic materials, neodymium magnets and strontium hexaferrite.
E-mail: kursaticin@ktu.edu.tr

Bülent ÖZTÜRK was born in Trabzon. He received his B.Sc., M.Sc. and Ph.D. degrees in Mechanical Engineering from KTU, in 1994, 1998, and 2004, respectively. He also worked as post-doctoral researcher at mechanical engineering in Virginia Commonwealth University, USA during 2010-2011. He is currently associate professor in Metallurgical and Materials Engineering Department at KTU. His current research interests are tribology, composite materials, powder metallurgy and mechanical properties.
E-mail: bozturk@ktu.edu.tr

Special Issue Article | ICADET 2017[C]

Turkish Journal of Electromechanics & Energy

ISSN-2547-975X

Eigenvalue Analysis of Mindlin Plates Resting on Elastic Foundation

Yaprak Itır Özdemir[1]

[1]Department of Civil Engineering, Karadeniz Technical University, 61080, Trabzon, Turkey

Received: 13 October 2017; Accepted: 22 December 2017; Published: 30 December 2017

Turk J Electrom Energy Vol: 2 No: 2 Page: 20-25 (2017)

SLOI: http://www.sloi.org/

Correspondence E-mail: yaprakozdemir@hotmail.com

ABSTRACT The purpose of this paper is to study free vibration analysis of thick plates resting on Winkler foundation using Mindlin's theory with shear locking free fourth order finite element, to determine the effects of the thickness/span ratio, the aspect ratio, subgrade reaction modulus and the boundary conditions on the frequency parameters of thick plates subjected to free vibration. In the analysis, finite element method is used for spatial integration. Finite element formulation of the equations of the thick plate theory is derived by using higher order displacement shape functions. A computer program using finite element method is coded in C++ to analyze the plates as free, clamped or simply supported along all four edges. In the analysis, 17-noded finite element is used. Graphs are presented that should help engineers designing of thick plates subjected to earthquake excitations. It is concluded that 17-noded finite element can effectively be used in the free vibration analysis of thick plates. It is also concluded that, the changes in the thickness/span ratio are more effective on the maximum responses considered in this study than the changes in the aspect ratio.

Keywords: Free Vibration Analysis, Winkler Foundation, Thick Mindlin Plates, Shear Locking Free Element, Finite Element Method

Cite this article: Y. I. Özdemir, Eigenvalue Analysis of Mindlin Plates Resting on Elastic Foundation, Turkish Journal of Electromechanics & Energy, 2(2), 20-25, (2017)

1. INTRODUCTION

The plates resting on elastic foundation is one of the most popular topics for the last decade in many engineering application. Winkler model, Pasternak model, Hetenyi model, Vlasov and Leont'ev model are the models used by the researchers to calculate the soil effects on the plate.

The dynamic behavior of thick plates has been investigated by many researchers [1, 2, 3, 4, 5]. In many cases, numerical solution can have lack of convergence, which is known as "shear-locking". This problem can be avoided by increasing the mesh size, i.e. using finer mesh, but if the thickness/span ratio is "too small", convergence may not be achieved even if the finer mesh is used for the low order displacement shape functions.

In order to avoid shear locking problem, different methods and techniques, such as reduced and selective reduced integration, the substitute shear strain method, etc., are used by several researchers [6, 7, 8, 9, 10]. The same problem can also be prevented by using higher order displacement shape function [11]. Vibration analysis made by [12], they presented natural frequencies and modes of rhombic Mindlin plates. Özdemir and Ayvaz [13] studied shear locking free earthquake analysis of thick and thin plates using Mindlin's theory. However, no references have been found in literature for the free vibration analysis of thick plates resting on Winkler foundation by using fourth order 17-noded finite element.

The aim of this paper is to analyze eigenvalue analysis of thick plates resting on Winkler foundation using Mindlin's theory with shear locking free fourth order finite element, to determine the effects of the thickness/span ratio, the aspect ratio, subgrade reaction modulus and the boundary conditions on the frequency parameters of thick plates with free vibration. In the study C++ computer program used for analyzing the plates which are free, clamped or simply supported along all four edges. In the code, the finite element method is used for spatial integration. Finite element formulation of the equations of the thick plate theory is derived by using fourth order displacement shape functions. In the

[C]*Initial version of this paper was selected from the proceedings of International Conference on Advanced Engineering Technologies (ICADET 2017) which was held in September 21-23, 2017, in Bayburt, TURKEY; and was subjected to peer-review process prior to its publication.*

analysis, 17-noded finite element is used to construct the stiffness and mass matrices since shear locking problem does not occur if this element is used in the finite element modelling of the thick and thin plates [11]. For this element in the analysis no matter what the mesh size is at the plate unless it is less than 4x4. This is a new element, details of its formulation are presented in [11] and this is the first time this element is used in the free vibration analysis of thick plates. If this element is used in an analysis, it is not necessary to use finer mesh.

2. MATHEMATICAL MODEL

The governing equation for a flexural plate (Fig. 1) subjected to free vibration without damping can be given as;

$$[M]\{\ddot{\omega}\}+[K]\{\omega\}=0 \tag{1}$$

where [K] and [M] are the stiffness matrix and the mass matrix of the plate, respectively, ω and $\ddot{\omega}$ are the lateral displacement and the second derivative of the lateral displacement of the plate with respect to time, respectively.

The total strain energy of plate-soil-structure system (see Fig. 1) can be written as;

$$\Pi=\Pi_P+\Pi_S+V \tag{2}$$

where Π_P is the strain energy in the plate,

$$\prod_p=\frac{1}{2}\int_A\begin{pmatrix}-\frac{\partial\varphi_x}{\partial x} & \frac{\partial\varphi_y}{\partial y} & -\frac{\partial\varphi_x}{\partial y}+\frac{\partial\varphi_y}{\partial x}\end{pmatrix}^T E_\kappa \begin{pmatrix}-\frac{\partial\varphi_x}{\partial x} & \frac{\partial\varphi_y}{\partial y} & -\frac{\partial\varphi_x}{\partial y}+\frac{\partial\varphi_y}{\partial x}\end{pmatrix} d_A + \frac{k}{2}\int_A\begin{pmatrix}-\varphi_x+\frac{\partial w}{\partial x} & \varphi_y+\frac{\partial w}{\partial y}\end{pmatrix}^T E_\gamma \begin{pmatrix}-\varphi_x+\frac{\partial w}{\partial x} & \varphi_y+\frac{\partial w}{\partial y}\end{pmatrix} d_A \tag{3}$$

where Π_S is the strain energy stored in the soil,

$$\prod_s=\frac{1}{2}\int_0^H\int_{-\infty}^{\infty}\int_{-\infty}^{\infty}\sigma_{ij}\varepsilon_{ij} \tag{4}$$

and V is the potential energy of the external loading;

$$V=-\int_A\bar{q}wd_A \tag{5}$$

In this equation E_κ and E_γ are the elasticity matrix and $\bar{q}$ shows applied distributed load.

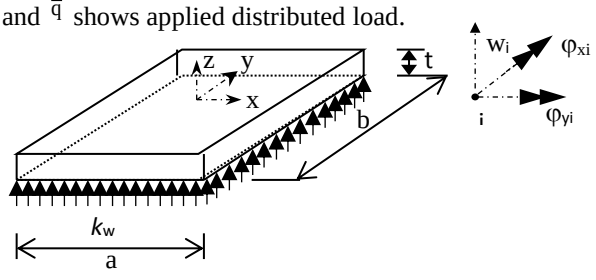

Fig. 1. The sample plate used in this study

2.1. Creating of the Stiffness Matrix

The total strain energy of the plate-soil system according to Eq. (2) is;

$$Ue=\frac{1}{2}\int_A\begin{pmatrix}-\frac{\partial\varphi_x}{\partial x} & \frac{\partial\varphi_y}{\partial y} & -\frac{\partial\varphi_x}{\partial y}+\frac{\partial\varphi_y}{\partial x}\end{pmatrix}^T E_\kappa \begin{pmatrix}-\frac{\partial\varphi_x}{\partial x} & \frac{\partial\varphi_y}{\partial y} & -\frac{\partial\varphi_x}{\partial y}+\frac{\partial\varphi_y}{\partial x}\end{pmatrix} d_A + \frac{k}{2}\int_A\begin{pmatrix}-\varphi_x+\frac{\partial w}{\partial x} & \varphi_y+\frac{\partial w}{\partial y}\end{pmatrix}^T E_\gamma \begin{pmatrix}-\varphi_x+\frac{\partial w}{\partial x} & \varphi_y+\frac{\partial w}{\partial y}\end{pmatrix} d_A + \frac{1}{2}\int_A(w_{x,y})^T K(w_{x,y})d_A \tag{6}$$

At this equation the first and second part gives the conventional element stiffness matrix of the plate, $[kp^e]$, differentiation of the third integral with respect to the nodal parameters yields a matrix, $[kw^e]$, which accounts for the axial strain effect in the soil. Thus the total energy of the plate-soil system can be written as;

$$Ue=\frac{1}{2}\{w_e\}^T([k_p^e]+[k_w^e])\{w_e\}d_A \tag{7}$$

Where;

$$\{w_e\}=\begin{bmatrix}w_1 & \varphi_{y1} & \varphi_{x1} & \cdots & w_n & \varphi_{yn} & \varphi_{xn}\end{bmatrix}^T \tag{8}$$

Assuming that in the plate of Fig. 1 u and v are proportional to z and that w is the independent of z, one can write the plate displacement at an arbitrary x, y, z in terms of the two slopes and a displacement as follows;

$$ui=\{w, v, u\}=\{w_0(x,y,t), z\varphi_y(x,y,t), -z\varphi_x(x,y,t)\} \tag{9}$$

where w_0 is average displacement of the plate, and φ_x and φ_y are the bending slopes in the x and y directions, respectively.

The nodal displacements for 17-noded quadrilateral serendipity element (MT17) (Fig. 2) can be written as follows;

$$w=\sum_1^{17}h_iw_i,\ v=z\varphi y=z\sum_1^{17}h_i\varphi_{yi},\ u=-z\varphi x=-z\sum_1^{17}h_i\varphi_{xi}\quad i=1,\ldots,17\ \text{for}\ 17\text{-nodedelement}, \tag{10}$$

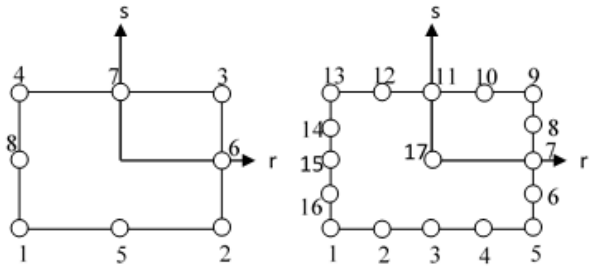

Fig. 2. 8- (second order), and 17-noded (fourth order) quadrilateral finite elements used in this study

The displacement function chosen for this element is;

$$w = c_1 + c_2 r + c_3 s + c_4 r^2 + c_5 rs + c_6 s^2 + c_7 r^2 s + c_8 rs^2 + c_9 r^3 + c_{10} r^3 s + c_{11} rs^3 + c_{12} s^3 + c_{13} r^2 s^2 + c_{14} r^4 + c_{15} r^4 s + c_{16} rs^4 + c_{17} s^4. \quad (11)$$

From this assumption, it is possible to derive the displacement shape function to be [11];

$$h = [h_1, \ldots, h_{17}]. \quad (12)$$

Then, the strain-displacement matrix [B] for this element can be written as follows [13]:

$$[B] = \begin{bmatrix} 0 & 0 & -\frac{\partial h_i}{\partial x} & \cdots \\ 0 & \frac{\partial h_i}{\partial y} & 0 & \cdots \\ 0 & \frac{\partial h_i}{\partial x} & -\frac{\partial h_i}{\partial y} & \cdots \\ \frac{\partial h_i}{\partial x} & 0 & -h_i & \cdots \\ \frac{\partial h_i}{\partial y} & h_i & 0 & \cdots \end{bmatrix}_{5x51}$$

$$i = 1, \ldots, 17 \text{ for } 17\text{-node element} \quad (13)$$

The stiffness matrix for MT17 element can be obtained by the following equation [14].

$$[K] = \int_A [B]^T [D][B] dA. \int_{-1}^{1}\int_{-1}^{1} [B]^T [D][B] |J| dr ds \quad (14)$$

which must be evaluated numerically [10].

As seen from Eq. (14), in order to obtain the stiffness matrix, the strain-displacement matrix, [B], and the flexural rigidity matrix, [D], of the element need to be constructed.

The flexural rigidity matrix, [D], can be obtained by the following equation.

$$[D] = \begin{bmatrix} E_k & 0 \\ 0 & E_\gamma \end{bmatrix} \quad (15)$$

In this equation, $[E_k]$ is of size 3x3 and $[E_\gamma]$ is of size 2x2. $[E_k]$, and $[E_\gamma]$ can be written as follows [16, 17]:

$$E_k = \frac{t^3}{12} \begin{bmatrix} \frac{E}{(1-\nu^2)} & \frac{\nu E}{(1-\nu^2)} & 0 \\ \frac{\nu E}{(1-\nu^2)} & \frac{E}{(1-\nu^2)} & 0 \\ 0 & 0 & \frac{E}{2(1-\nu)} \end{bmatrix};$$

$$E_\gamma = k t \begin{bmatrix} \frac{E}{2.4(1+\nu)} & 0 \\ 0 & \frac{E}{2.4(1+\nu)} \end{bmatrix} \quad (16)$$

where *E,* υ, and *t* are modulus of the elasticity, Poisson's ratio, and the thickness of the plate, respectively, *k* is a constant to account for the actual non-uniformity of the shearing stresses. By assembling the element stiffness matrices obtained, the system stiffness matrix is obtained.

2.2. Evaluation of the Mass Matrix

The formula for the consistent mass matrix of the plate may be written as;

$$M = \int_\Omega H_i^T \mu H_i d\Omega \quad (17)$$

In this equation, μ is the mass density matrix of the form [Tedesco et al., 1999]

$$\mu = \begin{bmatrix} m_1 & 0 & 0 \\ 0 & m_2 & 0 \\ 0 & 0 & m_3 \end{bmatrix}, \quad (18)$$

where $m_1 = \rho pt$, $m_2 = m_3 = \frac{1}{12}(\rho_p t^3)$, and ρp is the mass densities of the plate, and H_i can be written as follows,

$$H_i = \begin{bmatrix} dh_i/dx & dh_i/dy & h_i \end{bmatrix} \qquad i = 1 \ldots 17. \quad (19)$$

It should be noted that the rotation inertia terms are not taken into account. By assembling the element mass matrices obtained, the system mass matrix is obtained.

2.3. Evaluation of Frequency of Plate

The formulation of lateral displacement, w, can be given as motion is sinusoidal;

$$w = W \sin \omega t \quad (20)$$

Here ω is the circular frequency. Substitution of Eq. (20) and its second derivation into Eq. (1) gives expression as;

$$[K - \omega^2 M]\{W\} = 0 \quad (21)$$

Eq. (21) is obtained to calculate the circular frequency, ω, of the plate. Then natural frequency can be calculated with the formulation below;

$$f = \omega / 2\pi \quad (22)$$

3. NUMERICAL EXAMPLES

3.1. Data for Numerical Examples

In the light of the results given in references [17, 18], the aspect ratios, b/a, of the plate are taken to be 1, 1.5, and 2.0. The thickness/span ratios, t/a, are taken as 0.01, 0.05, 0.1, 0.2, and 0.3 for each aspect ratio. The shorter span length of the plate is kept constant to be 10 m. The mass density, Poisson's ratio, and the modulus of elasticity of the plate are taken to be 2.5 kN.s^2/m^2, 0.2, and 2.7x10^7 kN/m^2. Shear factor k is taken to be 5/6. The subgrade reaction modulus of the Winkler-type foundation is taken as 500 and 5000 kN/m^3.

Rather than starting from the finite element network size for the sake of correctness of the results, the network size required to achieve the desired accuracy is determined before delivering any results. This analysis was performed separately for the mesh size. It has been concluded that when using 4x4 mesh size 10 m x 10 m plate with 17-noded elements, the results have acceptable error. As in the case of the square plate, the lengths of the each element are kept constant in the x and y directions.

In order to show that the mesh density used in this paper is enough to obtain correct results, the first six frequency parameters of the thick plate with b/a=1 and t/a=0.05 is presented in Table 1 by comparing with the result obtained SAP2000 program and the results Özgan and Daloğlu [2015]. In this study Özgan and Daloğlu used 4-noded and 8-noded quadrilateral finite element with 10x10 and 5x5 mesh size. It should be noted that the results presented for MT17 element are obtained by using equally spaced 2x2 mesh size. As seen from Table 1, the results obtained by using 17-noded quadrilateral finite element have excellent agreement with the results obtained by [18] and SAP2000 software even if 2x2 mesh size is used for MT17 element.

3.2. Results

The first six frequency parameters of thick plate resting on Winkler foundation with free edges are compared with the same thick plate modeled by [18] and SAP2000 program and it is presented in Table 1. The subgrade reaction modulus of the Winkler-type foundation for this example is taken to be 5000 kN/m^3. This thick plate is modeled with MT17 element 2x2 mesh size for b/a=1.0, t/a=0.05 ratios.

As seen from Table 1, the values of the frequency parameters of these analyses are so close even if this study mesh size is so poor. Then parameter such as aspect ratio, b/a, thickness/span ratio, t/a where taken in a wider range, and analyses were performed.

Table 1.The first five natural frequency parameters of plates for b/a=0.1 and t/a=0.05

$\lambda_i=\omega^2$	[18]	This Study	SAP2000
	PBQ8(FI)	MT17 (4 element)	
1	3990.42	4002.41	4000.00
2	3990.42	4002.41	4000.00
3	4000.40	4021.55	4000.00
4	8676.00	8650.67	8619.60
5	13957.64	13789.50	13292.31
6	17252.34	16939.10	16380.24

Table 2. Effects of aspect ratio and thickness/span ratio on the first six frequency parameters of the thick free plates resting on elastic foundation

Subgrade reaction modulus k=500								
k	b/a	t/a	$\lambda=\omega^2$					
			λ_1	λ_2	λ_3	λ_4	λ_5	λ_6
500	1.0	0.05	456.73	456.73	469.98	5048.72	10235.7	13366.9
		0.10	235.42	235.42	283.12	17448.0	37556.4	49322.0
		0.20	171.76	171.76	175.32	58681.1	126694.	164490.
		0.30	149.09	149.09	179.38	109100.	229933.	295362.
	1.5	0.05	458.49	464.03	470.14	2492.94	2660.49	10937.2
		0.10	241.45	259.74	289.49	7970.41	8878.92	39117.9
		0.20	170.28	173.06	174.51	27346.7	31896.0	127052.
		0.30	153.01	163.56	183.08	52430.1	63261.4	225607.
	2.0	0.05	459.37	466.66	470.22	1161	1588.82	5784.55
		0.10	244.46	271.13	292.64	3031.39	4557.16	20388.1
		0.20	169.53	171.92	174.46	10730.8	15546.2	68560.2
		0.30	154.97	170.85	184.92	22168.0	30127.2	126587.
	3.0	0.05	460.25	468.61	470.30	603.44	951.50	1519.07
		0.10	247.47	281.97	295.67	825.36	2129.95	4437.42
		0.20	168.79	170.78	173.44	2333.89	6956.53	15815.4
		0.30	156.93	177.91	186.77	4859.98	13529.7	32166.7

The first six frequency parameters of thick plates resting on Winkler foundation considered for different aspect ratio, b/a, thickness/smaller span ratio, t/a, are presented in Table 2 for with free edges and in Table 3 for the thick simply supported plates. To see the effects of these changes on the first six frequency parameters, they are also presented in Figures 3 for the thick free plates, in Figures 4 for the thick simply supported plates.

As it can be seen from Tables 2, and 3, and Figures 3, and 4, the values of the first three frequency parameters for a constant value of t/a increase as the aspect ratio, b/a, increases up to the 3rd frequency parameters, but after the 3rd frequency parameter, the values of the frequency parameters for a constant value of t/a decrease as the aspect ratio, b/a, increases.

As also seen from Tables 2, and 3, and Figures. 3, and 4, the values of the first three frequency parameters for a constant value of b/a decrease as the thickness/span ratio, b/a, increases up to the 3rd frequency parameters, but after the 3rd frequency parameters, the values of the frequency parameters for a constant value of b/a increase as the thickness/span ratio, t/a, increases.

The increase in the frequency parameters with increasing value of b/a for a constant t/a ratio reduces for larger values of b/a up to the 3rd frequency parameters. After the 3rd frequency parameters, the decrease in the frequency parameters with increasing value of b/a for a constant t/a ratio reduces for larger values of b/a.

Table 3. Effects of aspect ratio and thickness/span ratio on the first six frequency parameters of the thick simply supported plates resting on elastic foundation

Subgrade reaction modulus k=500								
k	b/a	t/a	$\lambda = \omega^2$					
			λ_1	λ_2	λ_3	λ_4	λ_5	λ_6
500	1.0	0.05	9047.4	53796.	53796.	132323.	208613.	208895.
		0.10	31594.4	186728.	186728.	431328.0	675755.9	678833.0
		0.20	100289.	524820.	524820.	1078904.	1617046.	1635881.
		0.30	177442.	817902.	817902.	1562458.	2233537.	2283380.
	1.5	0.05	5015.82	17094.0	43388.9	54027.36	71060.68	133204.5
		0.10	17329.0	60561.6	154092.	188245.0	242603.2	436597.4
		0.20	57457.2	186916.	449433.	530921.1	658117.1	1095658.
		0.30	106026.	318024.	715938.	828749.9	1001294.	1585462.
	2.0	0.05	3912.42	9138.54	23276.2	39998.98	54142.96	54143.89
		0.10	13407.9	32257.5	82636.3	143304.1	189004.4	189006.5
		0.20	45541.0	103507.	250665.	424221.4	533149.2	533974.8
		0.30	85976.3	183477.	417846.	682308.0	830510.8	834182.7
	3.0	0.05	3220.63	5043.23	9169.12	17200.91	31325.02	37650.27
		0.10	10941.0	17534.1	32481.8	61320.90	111087.0	135748.4
		0.20	38015.9	58510.7	104603.	190395.9	330316.7	406397.0
		0.30	73378.6	108073.	185541.	324384.2	539235.3	658701.9

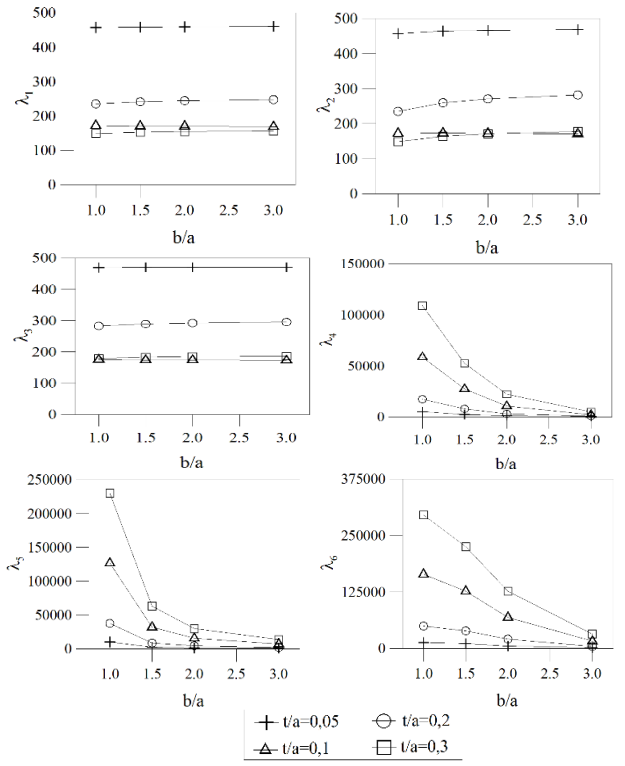

Fig. 3. Effects of aspect ratio and thickness/span ratio on the first six frequency parameters (λ_1 to λ_6) of the thick free plates with subgrade reaction modulus k=500,

The changes in the frequency parameters with increasing value of b/a for a constant t/a ratio is larger for the smaller values of the b/a ratios. Also, the changes in the frequency parameters with increasing value of b/a for a constant t/a ratio is less than that in the frequency parameters with increasing t/a ratios for a value of b/a.

These observations indicate that the effects of the change in the t/a ratio on the frequency parameter of the plate are generally larger than those of the change in the b/a ratios considered in this study.

As it can also be seen from Tables 2, and 3, and Figures 3, and 4 that the curves for a constant value of b/a ratio are fairly getting closer to each other as the value of t/a increases up to the 3rd frequency parameters. This shows that the curves of the frequency parameters will almost coincide with each other when the value of the ratio of t/a increases more. After the 3rd frequency parameters, the curves for a constant value of t/a ratio are getting closer to each other as the value of b/a increases.

In other words, up to the 3rd frequency parameters, the increase in the t/a ratio will not affect the frequency parameters after a determined value of t/a. After the 3rd frequency parameters, the increase in the b/a ratio will not affect the frequency parameters after a determined value of b/a. It should be noted that the increase in the frequency parameters with increasing t/a ratios for a constant value of b/a ratio gets larger for big values of the frequency parameters.

These observations indicate that the effects of the change in the t/a ratio on the frequency parameter of the thick plates simply supported or clamped along all four edges are always larger than those of the change in the aspect ratio.

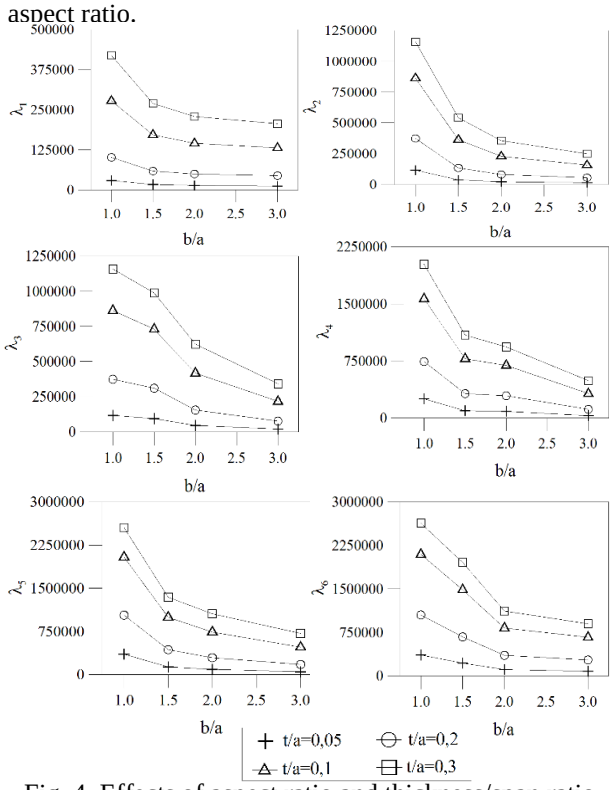

Fig. 4. Effects of aspect ratio and thickness/span ratio on the first six frequency parameters (λ_1 to λ_6) of the thick simply supported plates with subgrade reaction modulus k=500,

4. CONCLUSION

The aim of this article is to study the parametric eigenvalue analysis of thick plates using Mindlin theory using high-order finite elements and to determine the effects of thickness/ span ratio, aspect ratio and boundary conditions on the linear response of applied thick plates.

As a result, free vibration analyze of the thick plates were done by using *p* version serendipity element, and the coded program on the purpose is effectively used. In addition, the following conclusions can also be drawn from the results obtained in this study.

The frequency parameters increases with increasing b/a ratio for a constant value of t/a up to the 3rd frequency parameters, but after that those decrease with increasing b/a ratio for a constant value of t/a.

The frequency parameters decreases with increasing t/a ratio for a constant value of b/a up to the 3rd frequency parameters, but after that those increases with increasing t/a ratio for a constant value of b/a.

The effects of the change in the t/a ratio on the frequency parameter of the thick plate are generally larger than those of the change in the b/a ratios considered in this study.

References

[1] A. C. Ugural, Stresses in Plates and Shells, McGraw-Hill, New York, (1981).

[2] R. M. Grice, R. J. Pinnington, Analysis of the flexural vibration of a thin-plate box using a combination of finite element analysis and analytical impedances, J. Sound Vib., 249(3), 499-527, (2002).

[3] T. S. Lok, Q. H. Cheng, Free and forced vibration of simply supported, orthotropic sandwich panel, Comput. Struct., 79(3), 301-312, (2001).

[4] W. J. Si, K. Y. Lam, S. W. Gang, Vibration analysis of rectangular plates with one or more guided edges via bicubic B-spline method, Shock Vib., 12(5), (2005).

[5] Y. Ayvaz, A. Durmuş, Earthquake analysis of simply supported reinforced concrete slabs, J. Sound Vib., 187(3), 531-539, (1995).

[6] E. Hinton, and HC. Huang, A Family of Quadrilateral Mindlin Plate Element with Substitute Shear Strain Fields, Computer and Structures, 23(3), 409-431, (1986).

[7] O. C. Zienkiewich, R. L. Taylor, and J. M. Too, Reduced integration technique in general analysis of plates and shells, Int. J. for Numerical Methods in Engineering, 3, 275-290, (1971).

[8] P. G. Bergan, and X. Wang, Quadrilateral Plate Bending Elements with Shear Deformations, Comput. Struct., 19(1-2), 25-34, (1984).

[9] T. A. Ozkul and U. Ture, The transition from thin plates to moderately thick plates by using finite element analysis and the shear locking problem, Thin-Walled Structures, 42, 1405-1430, (2004).

[10] T. J. R. Hughes, R. L. Taylor, and W. Kalcjai, Simple and efficient element for plate bending, Int. J. for Numerical Methods in Engineering, 11, 1529-1543, (1977).

[11] Y. I. Özdemir, S. Bekiroğlu, and Y. Ayvaz, Shear locking-free analysis of thick plates using Mindlin's theory, Struct. Eng. Mech. 27(3), 311-331, (2007).

[12] K. K. Raju, E. Hinton, Natural frequencies and modes of rhombic Mindlin plates, Earhq. Eng. Struct. Dyn., 8, 55-62, (1980).

[13] Y. I. Özdemir, Y. Ayvaz, Shear Locking-Free Earthquake Analysis of Thick and Thin Plates Using Mindlin's Theory, Struct. Eng. Mech. 33(3), 373-385, (2009).

[14] R. D. Cook, D. S. Malkus, and E. P. Michael, Concepts and Applications of Finite Element Analysis. John Wiley & Sons, Inc., Canada, (1989).

[15] K. J. Bathe, Finite Element Procedures, Prentice Hall, Upper Saddle River, New Jersey, (1996).

[16] W. Weaver, and P. R. Johnston, Finite elements for structural analysis, Prentice Hall, Englewood Cliffs; New Jersey, (1984).

[17] Y. I. Özdemir, Development of a higher order finite element on a Winkler foundation, Finite Elem. Anal. Des., 48, 1400-1408, (2012).

[18] K. Özgan, and A. T. Daloglu, Free vibration analysis of thick plates resting on Winkler elastic foundation, Challenge J. Struct. Mech., 1(2), 78-83, (2015).

Biography

Yaprak Itır Özdemir was born in 1975. She received her B.Sc. Degree in Civil Engineering from Karadeniz Technical University in 1997, Trabzon, Turkey. She worked in private sector a couple of years as a civil engineer. In 2001, she received her M.Sc. degree and 2007 her Ph.D. degree from Karadeniz Technical University, Trabzon, Turkey. She became an associate professor in 2012. Özdemir is currently an associate professor at Karadeniz Technical University. Her research interests include thick plates, antique engineering, and structural engineering.